Faculty 13 Physics
Frankfurt Institute for Advanced Studies

Master's Thesis

Diffusive Homeostasis in a Self-Organizing Recurrent Neural Network

Spatially dependent Interaction as a Determinant of Neural Activity and Plasticity

Fabian Schubert
Matriculation Number: 4282141

Thesis Supervisor: Prof. Dr. Jochen Triesch

February 6, 2017

Statutory Declaration

I hereby declare that I authored this thesis independently and that I have not used other than the declared sources/resources. I explicitly marked all material which has been quoted either literally or by content from the used sources. I further declare that neither the thesis, nor any section of it, was used as a study achievement for any other graded or ungraded exam.

Contents

1 Introduction

1.1 Homeostasis in the Nervous System

Among other functional roles of the mammalian central nervous system, it is involved in maintaining crucial properties of the body in a functional regime. Some examples regarding the organism as a whole are e.g. body temperature and blood pressure, both being controlled by hypothalamus [1, p. 484]. The term *homeostasis* entailing these regulatory mechanisms was first introduced by Walter C. Cannon in 1932 [2, 3]. In more recent years, experimental studies have found evidence for processes within the brain that do not function as a regulatory control for certain aspects of the body, but as a homeostatic control of neural activity itself [4, 5]. Many processes underlying this self-regulatory behavior have been found up till now, and many different biophysical interdependencies have shown to play a role. This diversity makes comparability of these mechanisms a rather difficult task. On a relatively general level though, experiments have revealed two main types of neuronal regulation: synaptic homeostatic plasticity and intrinsic homeostasis [6].

The notion of synaptic homeostatic plasticity subsumes the observation that neurons being more or less active than a certain set point of mean activity are regulated by means of their incoming synaptic weights. Theoretical and experimental studies have suggested that this type of regulation is taking place in a multiplicative manner, thereby retaining proportions between individual synaptic strengths [7]. Furthermore, one can regard this form of plasticity as an antagonist to other aspects of synaptic plasticity that affect synaptic strengths in an activity dependent, hebbian fashion. Forms of regulation belonging to intrinsic homeostasis alter the neurons' capability of spiking upon external input by changing "intrinsic" properties of the nerve cell. More precisely, a neurons' ability to form an action potential can change by modifying the conductance of ion channels in its cell membrane [8, p. 156].

Theoretical models of homeostasis are generally based on a form of feedback control. In control theory, this is also known as a *closed loop control*. All these systems include a number of necessary functional compartments, which will be briefly introduced in the following. Concepts and terms were taken from [9, p. 59-64].

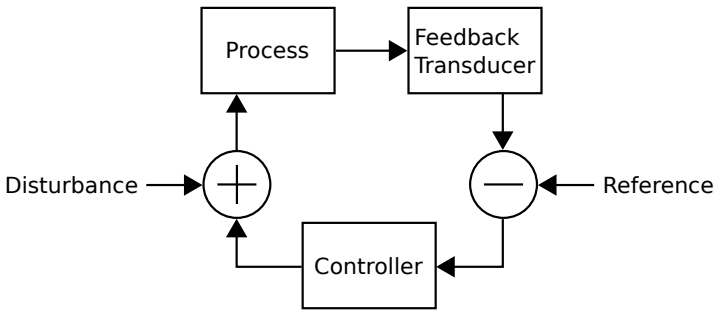

Figure 1: Schematic illustration of a closed loop control as described in Section 1.1.1

1.1.1 Theory of Control Systems

Generally, a closed loop control must contain some *process* that is to be regulated. Despite its potential internal complexity, its functional role in the context of a feedback system is to simply generate a time-dependent output based on the history of a time-dependent input. This output is what one wishes to control and regulate by means of the feedback loop and thus represents the signal that is further processed. However, it might not be possible to directly quantify this desired output in terms of some internal state of the process. For example, the firing rate of a neuron is an abstract quantity, which can not be *directly* related to some neuronal state variable. Consequently, it might be necessary to transform the actual output of the process into a different signal by a *feedback transducer*. As a necessary next step, the (potentially transformed) output is fed into a *comparator*, which, unsurprisingly, compares the given output of the process to some given target or *reference*, typically by subtraction. Note that this reference can but does note have to be a time-dependent signal. However, the term *homeostasis* generally refers to a fixed reference, while implementations with a time dependent reference can be regarded as a form of *servomechanism*. The difference between reference and the feedback transducer's signal is known as the *error* signal. This error signal is given to a *controller*, which transforms this error signal into an appropriate input signal for the initially introduced process. Additionally, this is also the point in the control loop, where *external disturbances* come into play by being added to the input generated by the controller. We illustrated the described flow of feedback control in Figure 1. Based on the way the controller generates input for the dynamic process based on the error signal, one can classify control loops by three types:

- A *proportional controller* generates a signal that is proportional to the error signal it receives. The most important property of a proportional controller is that the stationary state of the control loop generally does not imply an error signal equal to zero.

- An *integrator controller* uses an integration over the past of the error signal to obtain its output. The stationary solution necessarily implies that the error signal is zero.

- A *differential controller* generates its output by means of the time derivative of the error signal. This type of controller can quickly react to momentary changes but does not compensate for sustained deviations of the error signal from zero.

It should be pointed out that these types of control mechanisms can be simultaneously used in a control system, e.g. through a linear combination. Furthermore, the presented terms refer to concepts of linear control theory. Thus, in the study of nonlinear feedback systems they only apply in a limited regime where a first order approximation of the system is sufficiently exact.

1.1.2 Error Signals and Controllers of Neuronal Homeostasis

When analyzing or modeling a biological system, a key step characterizing a control loop should be to identify the previously described compartments. While the functional separation illustrated in Figure 1 might seem intuitive and "straight forward", it is not obvious which physiological element should be attributed to a certain abstract element. As a start, we state that the process and its output controlled by homeostasis is the generation of action potentials and the resulting firing rate. As stated earlier, "firing rate" is an abstract quantity, requiring a feedback transducer to translate the neuron's spiking activity into a "sensible" quantity. In a nerve cell, this could be represented by e.g. the relation between the firing of action potentials and the temporary rise in Ca^{2+} concentration. An example for a homeostatic model making use of intracellular calcium concentration as a measure of spiking activity is the LeMasson-Abbott model [10]. More complex chains of activity encoding are of course possible, and we will introduce a recent model making additional use of the concentration of nitric oxide in Section 1.2 and 1.2.1. Given a representation of activity, its deviation from a reference value will cause other physiological compartments to affect the neuron's ability to generate action potentials. Referring to the concepts introduced in the previous section, one could then ask what type of control best resembles the actual neuronal control. The fact that neurons, whose firing rate was artificially increased or suppressed over a long time, can reliably tune

their activity back to the initial state (see e.g. [11]) rules out a purely differential type of control. The return to baseline under different disturbances seems to point towards an integral-like control. However, it is clear that a the ability of a biological system to encode the accumulation of an error signal is limited by the finite amount of available resources. For example, the conductance of an ion channel has natural upper and lower bounds that it can not surpass. We will pick up this issue in Section 5.2.1.

In any case, modeling homeostasis includes an error estimation, which requires setting some predefined target that the feedback control will attempt to achieve. This, of course, raises the question of how to choose these homeostatic targets. Experimental studies have found that neuronal populations exhibit a strong heterogeneity within their individual activity. In particular, many statistical analyses found evidence for a log-normal like distribution of firing rates [12, 13]. Following these results, one approach of modeling this feature would be to randomly distribute individual targets according to the aforementioned statistics. A problem of this procedure is the absence of any particular deeper physiological motivation or causation. In the light of this conceptual problem, one could, due to a lack of better knowledge, simply define a single global target of activity. However, it has been shown that heterogeneity of neural response onto external input within a population is crucial for efficient stimulus encoding [14]. Allowing for a broad distribution of activity thus has to be regarded an important compartment of models of cortical activity and structure.

A conceptual problem that one might consider is the fact that temporal fluctuations of activity are believed to be a major part of information transmission and processing within the brain [8, p. 123-150]. Homeostasis as described above could potentially override information by eliminating these fluctuations of activity. However, it is argued that homeostatic mechanisms act on time scales of hours to days and thus do not interfere with changes in activity taking place on the order of seconds or below [15].

Returning to the previous question, though the slowness of homeostatic adaptation might allow for temporal fluctuations of activity, it does not overcome the conceptual dichotomy between single cell homeostasis and persistent variability in spontaneous activity. Marder and Goaillard speculated that instead of a mechanism controlling activity on a single-cell level, one might consider the possibility of a "global sensor of network performance to provide error signals for tuning of the network" [16]. This concept was used by Sweeney et al. as the basic idea for the introduction of a diffusive, intercellular homeostatic mechanism, which will be introduced in the next section.

1.2 Diffusive Homeostasis

In this thesis, we examined *diffusive homeostasis* as a possible candidate to replace the previously used model of intrinsic plasticity. The idea and modeling of diffusive homeostasis was adopted from a paper by Sweeney et al. [17], which models neural tissue as a two-dimensional surface and a set of points representing the neurons' positions. The group of excitatory neurons acted as a point-source of nitric oxide (NO), as well as as a sensor for the NO-concentration at each individual position. The production and sensing of NO forms the basis of a feedback loop: The individual NO-readout is fed into a comparator which causes an appropriate change within the internal firing threshold of the neuron, in turn altering the neuron's firing rate. The control system is then closed by linking the rate of NO-production to the neuron's firing rate. The results by Sweeney et al. suggest that diffusive signaling could resolve the dichotomy between overall stability of firing activity and the need to allow flexibility among individual neurons' activities. Intuitively speaking, through the diffusive signal, each neurons receives a "mixture" of its own activity and its neighboring neurons. Thereby individual tuning of firing rates is suppressed while the overall population activity is kept at a constant level.

1.2.1 Nitric Oxide in the Nervous System

The model presented in [17] includes spatial interaction across excitatory neurons through the diffusion of nitric oxide (NO). Enzymes that are responsible for NO synthesis (NOS) are present in different areas of the body, namely being involved in the dilation of blood vessels (endothelial NOS, eNOS) , the immune system (inducible NOS, iNOS) and the CNS (neuronal NOS, nNOS) [18]. These Enzymes differ in their functionality and dependence on the presence of other molecules. In particular, nNOS is sensitive to the concentration of Ca^{2+} ionic Calcium [19, 20]. Because of its small molecular structure and electrical neutrality, nitric oxide that was synthesized in the nervous system can diffuse freely, which makes it a good candidate to be involved into form of diffusive intracellular communication [21].

Due to a depolarization of the membrane potential in the course of an action potential, voltage dependent Ca^{2+}-channels open, which causes a significant increase of the intracellular Calcium concentration (relative to the low concentration at rest) [22, p. 98-100]. A common theoretical description of voltage-dependent ion channels is provided by the Goldman-Hodgkin-Katz equations, see [22, p. 445-451]. As such, Ca^{2+} constitutes a causal link between spiking activity and the production of NO.

Experimental studies have also suggested that NO can act as an inhibitory diffusive signaling pathway, decreasing intrinsic excitability [23], or generally suggest a role of NO

in maintaining a functional state of activity [24]. In experiments upon neurons in the medial nucleus of the trapezoid body, Steinert et al. found that cells that were subject to NO-signaling by an external source exhibited an increment in outward K^+ current, which, due to its hyperpolarizing effect, can be regarded as a form of intrinsic inhibition.

1.3 Previous Research on the used Network Model

This thesis is based on earlier versions of a self-organizing recurrent neural network (SORN), in particular an implementation using leaky integrate-and-fire neurons (LIF-SORN) [25]. It was developed to model features of activity and topology of cortical networks, in particular L5 of the neocortex. In these previous implementations, a slow homeostatic mechanism was set up among excitatory neurons through an intrinsic adaptation of excitability. This led to the aforementioned problems of homeostatic control: Neural activity was tuned to a globally set target, allowing for no variability. Despite this limitation, the model has proven to be capable of showing a number of experimentally confirmed features. Zheng et al. have shown that distribution and dynamics of synaptic efficacies measured in rat hippocampus can be reproduced by a binary SORN using a discretized version of spike-timing-dependent plasticity and presynaptic normalization [26]. Based on this model, Miner et al. designed the LIF-SORN. This network reproduced the results of the binary SORN regarding self-organizing synaptic dynamics. Furthermore, it was able to explain the experimentally observed overrepresentation of bidirectional connections (see [27,28]) by means of a distance-dependent implementation of synaptic growth.

Generally, it has been argued that the set of rules used in these recurrent networks represent a realization of a minimum ensemble of functional compartments that are required in order to give rise to the desired capabilities. The network's ability of self-organization has not only been investigated in terms of network structure itself. It also successfully performed in unsupervised sequence-learning tasks, suggesting that the SORN can acquire and maintain associative memory [29].

1.4 Thesis Outline

Key aspects of this thesis include an analysis of the stability of the homeostatic control, followed by a comparison of features of the original LIF-SORN and the diffusive variant. We expect to observe a preservation of non-random features that have been found in the original LIF-SORN while incorporating a stronger variance within neural activity which has previously been suppressed by single-cell homeostasis. By an analytic approach we

parameter	**EE**	**EI**	**IE**	**II**
connection fraction	$\rightarrow 0.1$	0.1	0.1	0.5
initial connection strength	$0.0001mV$	$1.5mV$	$-1.5mV$	$-1.5mV$
conduction delay	$1.5ms$	$0.5ms$	$1.0ms$	$1.0ms$

Table 1: Parameters of synaptic connections.

predict activity within the network, thereby gaining an understanding of the relation between spatial structure and firing rates. In the face of possible new features within the network's structure, we clarify the causal relation between diffusive spatial interaction and synaptic topology.

2 Methods

2.1 Network Simulation

The Neural Network was simulated with the code used in [25], which makes use of the BRIAN spiking neural network simulator [30]. Thus, all following explanations regarding the simulation of neurons and mechanisms of synaptic plasticity are based on the methods described in the aforementioned paper.

Across a square area of $1000 \times 1000\ \mu m$, 400 excitatory LIF neurons and 80 inhibitory LIF neurons were assigned random positions. Before the start of the simulation, all but recurrent excitatory synapses were randomly generated until a desired connection fraction was reached. The connection probability between two neurons was calculated from a distant dependent Gaussian function with a standard deviation of 200 μm. For excitatory to inhibitory (EI) and inhibitory to excitatory (IE) synapses, the connection fraction was set to 0.1, and 0.5 for recurrent inhibitory synapses (II). These connections were kept at a fixed connection strength throughout the simulation. Furthermore, all synapses were simulated with a fixed (distance independent) conduction delay. See table 1 for a summary of parameters.

Recurrent excitatory synapses were subject to a number of plastic mechanisms to be described in the following.

2.1.1 Synaptic Plasticity

Synaptic Growth: At a rate of 1/sec, the random, distance dependent generation of new EE synapses was carried out n times, where n is taken from a normal distribution with mean 920 and standard deviation $\sqrt{920}$. This constant growth rate was tuned to achieve the desired target concentration of 0.1 (see 1).

Synaptic Pruning: At the same rate of 1/sec, EE synapses below a threshold of 0.000001 mV were removed, thus being added again to the set of "potential" connections from which the growth process draws new connections. Especially, they were temporarily excluded from STDP (see below).

Spike Timing Dependent Plasticity: An additive STDP rule was used as described e.g. in [31]. The change of weight between two neurons due to a pre- and postsynaptic spike (i $\rightarrow$ j) is defined as:

$$\Delta w_{ji} = \sum_k \sum_l W(t_j^l - t_i^k) \tag{1}$$

$$W(\Delta t) = A_+ exp(-\Delta t/\tau_+), \qquad \Delta t > 0 \tag{2}$$

$$W(\Delta t) = A_- exp(\Delta t/\tau_-), \qquad \Delta t < 0 \tag{3}$$

Indexes k and l refer to the k-th and l-th pre- and postsynaptic spike respectively. Parameters were chosen to approximate data from [32] and [33], namely $\tau_+ = 15ms$, $A_+ = 15mV$, $\tau_- = 30ms$ and $A_- = -7.5mV$. However, for the sake of reduction of computational effort, we used the "nearest neighbor" approximation, only calculating the effect of the most recent pre-post pair of spikes for potentiation and post-pre pair for depression, yielding roughly the same value as the full summation due to the fast decay times τ_+ and τ_- of the STDP-window.

Synaptic Normalization: Among other, experiments have suggested rescaling of synapses among individual postsynaptic neurons as a form of activity regulation in the brain: While preserving ratios of weights, the mean incoming connectivity is multiplicatively adjusted. While this general mechanism has been confirmed in many experiments, results differ regarding the question whether the target connectivity is dynamically changing in order to preserve a certain postsynaptic firing rate (homeostatic synaptic scaling), or whether it remains constant, effectively enforcing a synaptic normalization. Though the latter does not directly enforce a fixed level of activity, one can argue that in a balanced recurrent network, synaptic normalization still reduces the probability of very high or low firing rates caused by an above- or below-average total synaptic input.

We implemented synaptic normalization by calling a function once per sec., updating each w_{ji} from neuron i to neuron j as follows:

$$w_{ji} \rightarrow w_{ji} \frac{w_{total}}{\sum_i w_{ji}} \tag{4}$$

w_{total} was set to different values for each of the four types of connections between

the excitatory and inhibitory pool of neurons. Except for the dynamically populated EE-synapses, these values could be directly set in accordance with the previously given parameters of desired mean individual connection strength, size of the presynaptic population and connection fraction, by calculating $w_{total} = w_{mean} \cdot N_{presyn.pop} \cdot p_{connect}$. This yielded $w_{total,EI} = 60mV$, $w_{total,IE} = -12mV$, $w_{total,II} = -60mV$. $w_{total,EE}$ was set to $40mV$, corresponding to a mean synaptic weight of $1mV$, given a targeted EE-connection fraction of 0.1 and a population of 400 excitatory neurons.

Short Term Plasticity: As an additional stabilization of network activity, a short term plasticity (STP) mechanism acting on recurrent excitatory connections was implemented as presented in [34]. It modulates the effective synaptic weights by multiplying the value stored in the weight matrix w_{ji} by two dynamic variables x and u, $w_{ji}^{effective} = w_{ji} \cdot x \cdot u$, each synapse owning a pair (x, u). The dynamics of these variables are given by:

$$\dot{x} = \frac{1-x}{\tau_d},\ \dot{u} = \frac{U-u}{\tau_f} \tag{5}$$

Furthermore, each presynaptic spike causes a change of x and u by

$$x \to x - x \cdot u,\ u \to u + U(1-u) \tag{6}$$

If no spikes arrive, the system rests at $x \cdot u = U$. Otherwise, depending on the choice of τ_d and τ_f, one can achieve a weight modulation that is dominated by potentiation ($\tau_f \gg \tau_d$) or depression ($\tau_f \ll \tau_d$). As a rough approximation of the values that were experimentally observed [34], we chose $U = 0.04$, $\tau_d = 0.5s$ and $\tau_f = 2s$, giving it a tendency towards potentiation. However, one should keep in mind that for $U \in [0, 1]$, $x \cdot u \in [0, 1]$ always holds, thus the factor $x \cdot u$ has a generally diminishing effect. E.g., for our choice of variables, a Poisson input with a constant rate achieves the best synaptic transmission at a rate of $\sim 4.5Hz$, corresponding to $x \cdot u \approx 0.2$. "Potentiation" in this context refers to the fact that stronger input strengthens synaptic transmission *compared* to close to zero incoming spikes.

2.1.2 Neuron Model

We used a leaky integrate-and-fire-model for all neurons in the network, whose dynamics are described by a stochastic differential equation:

$$\tau_m dV = -(V - E_l)dt + \sqrt{\tau_m}\sigma dW \tag{7}$$

where V is the membrane potential, E_l is the equilibrium membrane potential, τ_m is the time constant of the membrane, σ is the standard deviation of the noise term and dW is the standard Wiener process. A neuron is said to spike when its membrane potential reaches the threshold voltage V_t. The voltage is then reset to V_r. A refractory period was not implemented. A presynaptic spike causes a simple (delayed, see Table 1) increment of the membrane potential of the postsynaptic neuron by $w_{ji}^{effective}$. Table 2 summarizes the aforementioned set of parameters.

parameter	**exc. neur.**	**inh. neur.**
$\mathrm{E_l}$	-60 mV	-60 mV
τ_m	20 ms	20 ms
$\mathrm{V_r}$	-70 mV	-60 mV
σ	$\sqrt{5}$ mV	$\sqrt{5}$ mV
$\mathrm{V_t}$	subject to IP	-58 mV

Table 2: Parameters of LIF neuron

2.1.3 Intrinsic Plasticity (IP)

Apart from dynamic processes within synapses which contribute to a stabilization of the network's activity, neurons possess internal mechanisms capable of maintaining a desired regime of activity. Regular-spiking cells are known to down-(up-)regulate their firing rate upon increased (decreased) input on a timescale of tens of milliseconds [35, 36]. Since our simulation did not incorporate any rapidly changing external drive, the network itself was not expected to exhibit fast changes of synaptic input, allowing us to neglect this feature. On the other hand, a similar form of adaption as a reaction on deprived or enhanced input can be observed on a timescale of hours to days [37]. In contrast to the former short-term adaption, which can be explained by a separation of timescales among different ionic currents in the cell [38, p. 252-256], in the latter case, [37] finds evidence that a long-term change in excitability can be attributed to an altered resistance of ionic channels. In the original LIF-SORN, a simple form of low intrinsic homeostasis was implemented by altering the neurons' firing threshold based on the deviation from a target firing rate. This thesis implemented a new model of slow intrinsic homeostasis, based on the work in [17]. The following section describes both models in further detail.

2.1.4 Modeling of Homeostatic Intrinsic Plasticity

Our original model of homeostatic control was described as an operation over discrete time steps $\Delta t = 0.1ms$, carried out for each excitatory neuron:

$$V_t \to V_t + \eta_{IP}(N_{spikes} - h_{IP}) \tag{8}$$

$$N_{spikes} \to 0 \tag{9}$$

where V_t is the firing threshold, η_{IP} an adaption rate and h_{IP} the desired number of spikes per time step. N_{spikes} is a variable, counting the number of spikes of the neuron within each interval. In a continuous, rate-based form, this update rule can as well be written as:

$$\dot{V}_t = \eta_{IP}(r - r_{IP}) \tag{10}$$

with r as the neuron's firing rate and $r_{IP} = h_{IP}/\Delta t$ the target firing rate. This feedback control indirectly drives the firing rate of each neuron towards r_{IP}: If $r > (<) r_{IP}$, V_t increases (decreases), reducing (increasing) the probability of a spike to occur.

The new diffusive homeostatic model by Sweeney et al. combined the empirical findings discussed in Section 1.2.1 into a set of differential equations:

$$\dot{Ca^{2+}}^i(t) = -\frac{{Ca^{2+}}^i}{\tau_{Ca^{2+}}} + Ca^{2+}_{spike} \sum_j \delta(t - t^i_{spike,j}) \tag{11}$$

$$\dot{nNOS}^i(t) = \frac{1}{\tau_{nNOS}} \left(\frac{{Ca^{2+}}^{i^3}}{{Ca^{2+}}^{i^3} + 1} - nNOS^i \right) \tag{12}$$

$$\dot{NO}(\mathbf{r}, t) = -\lambda NO + D\nabla^2 NO + \sum_i \delta^2(\mathbf{r} - \mathbf{r}^i_{neur}) \cdot nNOS^i \tag{13}$$

$$\dot{V}^i_t(t) = \frac{NO(\mathbf{r}^i_{neur}, t) - NO_0}{NO_0 \cdot \tau_{V_t}} \tag{14}$$

A depolarization within a nerve cell upon a spike-event t_{spike} causes a fixed inflow of ionic current Ca^{2+}_{spike}, which is modeled as an instantaneous increase of the Ca^{2+} concentration. Over time, the concentration decays exponentially by a time constant $\tau_{Ca^{2+}}$, see (11). Though Ca^{2+} currents can be described in a much more detailed fashion, it can be considered as a reasonable approximation [8, p. 198-203]. The influence of Ca^{2+} onto nNOS was modeled by Sweeney et al. through (12), using the Hill equation [39] to model a cooperative binding mechanism. The $nNOS$ production is then fed into the "pool" of nitric oxide via point sources located at the neurons' positions. Apart from the inflow and the diffusive term $D\nabla^2 NO$, an additional decay term was added to provide a stable finite NO concentration under constant neuronal activity.

parameter	value
r_{IP}	3 Hz
η_{IP}	0.1 mV
Ca^{2+}_{spike}	1
$\tau_{Ca^{2+}}$	10 ms
τ_{nNOS}	100 ms
D	default: 10000 $\mu m^2 s^{-1}$
λ	0.1 s^{-1}
τ_{V_t}	see section 3.1

Table 3: Parameters of homeostatic intrinsic plasticity.

Finally, the dynamics of the firing thresholds V_t^i were modeled such that the rate of change is proportional to the relative deviation of the NO concentration at the neurons' locations from a global target concentration NO_0.

Obviously, the appropriate choice of NO_0 is crucial for the goal of achieving and maintaining a certain level of activity. However, one cannot directly set a parameter of the model to the desired population activity, as it was the case for canonical intrinsic homeostasis. Rather, one needs to determine the average concentration *associated* with the desired activity and set it as a target concentration. Though it is possible to derive this relation in an analytic fashion, for practical purposes of the simulation, we let the system run with the previous homeostatic mechanism, still solving equation (11)-(13) until a steady mean over the concentrations at the neurons' positions was reached. This mean was then set to be the target concentration and we switched to diffusive homeostasis. Table 3 summarizes the choice of parameters that were introduced in this section. Diffusion parameters roughly match those measured in experiments [40].

2.2 Simulation of Diffusion

We solved (13) with the finite difference method on a grid $\mathbf{r}_{i,j}$ with a resolution of 100×100 points. Integration over time was carried out by a 4th-order Runge-Kutta method with a time step of $1ms$. On each time step, $\nabla^2 NO(\mathbf{r}_{i,j}) = \nabla^2 NO_{i,j}$ was approximated by

$$\nabla^2 NO_{i,j} \approx \frac{NO_{i+1,j} + NO_{i-1,j} + NO_{i,j+1} + NO_{i,j-1} - 4NO_{i,j}}{h^2} \tag{15}$$

where $h = L/100$ is the distance between neighbored grid points, determined by the length L of the square sheet and the resolution of the numeric grid. We implemented three possible boundary conditions into the simulation:

1.) Periodic boundary conditions:

$$NO_{i,N+1} = NO_{i,0} \tag{16}$$

$$NO_{N+1,i} = NO_{0,i} \tag{17}$$

$$NO_{i,-1} = NO_{i,N} \tag{18}$$

$$NO_{-1,i} = NO_{N,i} \tag{19}$$

with N being the grid resolution.

2.) Neumann boundary conditions, with $\nabla NO = (0, 0)$ at the boundaries:

$$NO_{i,N+1} = NO_{i,N-1} \tag{20}$$

$$NO_{N+1,i} = NO_{N-1,i} \tag{21}$$

$$NO_{i,-1} = NO_{i,1} \tag{22}$$

$$NO_{-1,i} = NO_{1,i} \tag{23}$$

3.) Dirichlet boundary conditions, with $NO = NO_{bound}$ at the boundaries.

If not explicitly marked differently, Neumann boundary conditions were used for most of the simulations. This decision relates to the previously described mechanism of synaptic growth: Neurons placed close to the edge of the sheet have a lower connection probability due to the absence of neighboring neurons in the direction perpendicular to the close-by border. It therefore models the synaptic growth within a square "cutout" of neural tissue. The Neumann boundary condition fits into this picture, since it allows a zero-flux condition at the borders. This is a reasonable assumption, because NO molecules cannot diffuse out of the tissue (unless they were placed in a fluid surrounding).

Equation (13) describes the influx of NO as a sum of scaled and spatially shifted Dirac functions. Apart from the question, whether this source term results in a well defined, finite solution at the neurons' positions (see section 4.2), it can only be modeled to a certain degree of accuracy, depending on the resolution of the numeric grid. In practice, we approximated the point sources of NO as an insertions at individual grid cells at a rate of $nNOS^i(t)/h^2$, where the normalizing divisor h^2 ensured the desired total influx per neuron. This numeric implementation required two additional constraints: First, all random neuron positions were confined to integer multiples of h in x- and y-direction. Second, to avoid redundancy and for physiological reasons, each grid cell could only hold one neuron at maximum. Both conditions combined led to an iterative generation of positions, where for each neuron a random number generator produced pairs of integers (n_x, n_y), each within $[0, N]$, until an unoccupied pair of integers was found and occupied,

moving on to the next neuron. Figure 2 shows an example of the resulting NO density throughout a simulation.

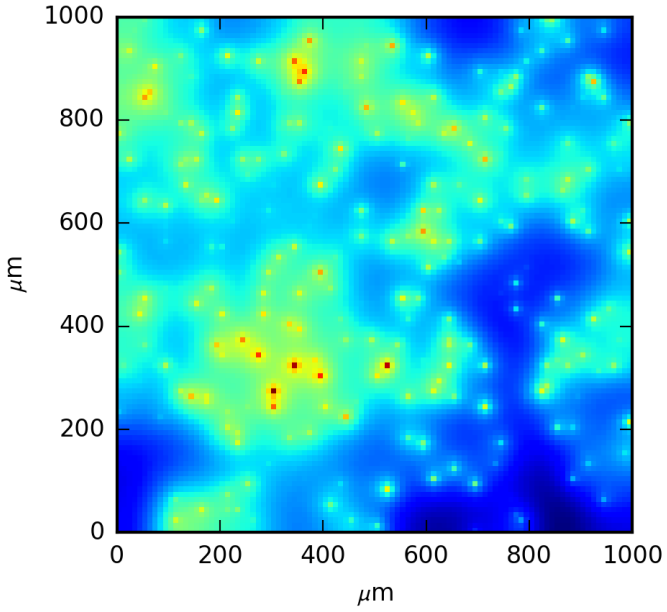

Figure 2: Example of NO-diffusion with 400 point sources of excitatory neurons.

3 Results

Since our main goal of the implementation of diffusive homeostasis was to allow the network to develop a broader distribution of firing rates across excitatory neurons compared to the original version of homeostasis, we first present the results of a comparison between features of the network activity in both variants in section 3.1. Following this is an analytic discussion of an instability we observed within the diffusive homeostatic feedback loop, see section 3.2. Furthermore, we compare topological features of the network under the influence of diffusive and non-diffusive homeostasis in section 3.4.

3.1 Activity Analysis

As a first attempt, we set the time constant of threshold adaptation in the diffusive homeostasis to 2500 ms, as given by [17]. Switching between non-diffusive/diffusive homeostasis after 750 seconds, Figure 3 shows the resulting dynamics of the population activity of the excitatory and inhibitory group, the average NO concentration at the excitatory neurons' positions and the average firing threshold within the excitatory group (inhibitory threshold was fixed, see table 2). Both homeostatic mechanisms managed to keep the excitatory population activity in the desired range of 3 Hz. However, what might appear to be slightly faster and stronger random fluctuations in the upper three plots of Figure 3, were in fact regular oscillations across all three depicted variables. While the oscillation amplitudes undergo a rather unpredictable course, the frequency remains at a constant level of $\simeq 0.5\,Hz$. This feature is also illustrated by the fact that the power spectra depicted in Figure 4 have a peak at the frequency that appeared to be dominant in Figure 3. The fact that the mean over all power spectra of excitatory thresholds differs from the power spectrum of the mean of these thresholds in its amplitude indicates that not all thresholds oscillate at the same phase. Still though, the overall shape of both spectra are equivalent. Although one might argue that - for the sake of practical purposes - regular oscillations of the NO concentration are not of much concern for the network as such, a periodically fluctuating firing rate is a qualitative feature requiring further inquiry. Rhythmic patterns of activity are a commonly observed phenomenon within the brain. Depending on the rate of oscillations, the location within the brain and the spatial scale over which they are observed, different physiological features are found to be responsible, leading to explanatory models at different levels of abstraction. On a microscopic, single-neuron level, a so-called slow after-hyper-polarization conductance explains the appearance of bursting behavior: A relatively short period of spiking activity is followed by a longer period of silence. This

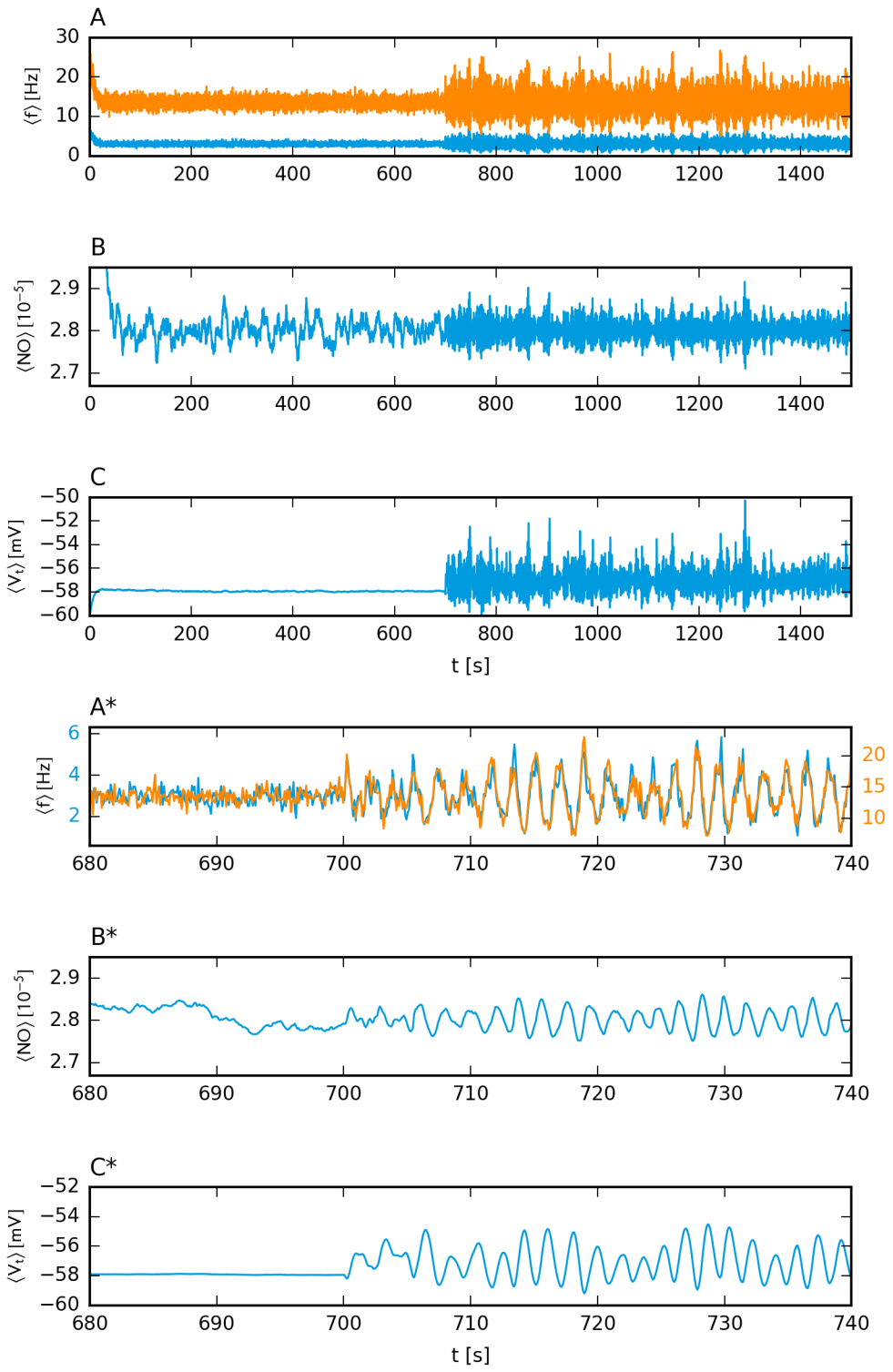

Figure 3: A/A*: Mean of excitatory (blue) and inhibitory (red) neuronal firing rate. B/B*: NO concentration averaged over readouts at excitatory neurons' positions. C/C*: Average excitatory firing threshold. Non-diffusive homeostasis was used for $0 - 700\,\mathrm{s}$, diffusive h. for $700 - 1500\,\mathrm{s}$. Target activity was $3\,\mathrm{Hz}$.

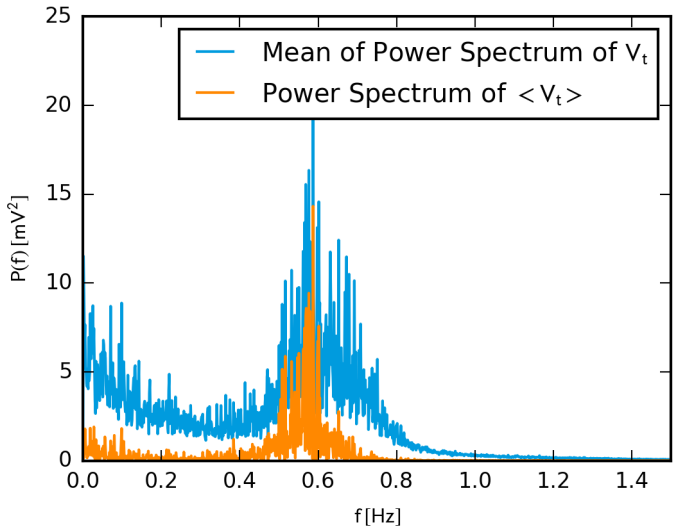

Figure 4: Blue: Mean of power spectrum over all excitatory thresholds. Red: Power spectrum of mean over all excitatory thresholds.

phenomenon can be modeled by a Ca^{2+}-dependent K^+-conductance. Upon the bursting period, Ca^{2+} concentration rises, prohibiting continuous spiking due to the activation of K^+ current until the Ca^{2+} concentration has returned to base-level [8, p. 203-207]. However, due to the simplicity of our neuron model, this type of oscillating activity can be ruled out as an explanation.

On a larger, rate-based level, dynamical models of interconnected excitatory and inhibitory groups can exhibit sustained oscillations of activity [8, p. 270]. As a simplest model, one can describe the dynamics of the excitatory and inhibitory populations as a two-dimensional dynamical system, representing the respective population rates r_e and r_i:

$$\tau_e \dot{r}_e = -r_e + \phi_e(r_e W_{ee} + r_i W_{ie}) \tag{24}$$

$$\tau_i \dot{r}_i = -r_i + \phi_i(r_e W_{ei} + r_i W_{ii}) \tag{25}$$

where τ_e and τ_i are time constants representing the rapidity of firing rate adaptation, ϕ_e and ϕ_i the respective transition functions between synaptic input and firing rate and W_{xy} the mean synaptic weight from population x to population y. A persistent oscillation then corresponds to a stable limit cycle in the 2-dimensional phase plane. According to the Poincaré-Bendixson theorem, such a limit cycle exists inside a region R if R contains no fixed points and if any trajectory whose starting points lies within R

is confined to R. The second condition is equivalent to the condition that for all points $\mathbf{r}_{edge}$ on the edge of R, the vector field $\dot{\mathbf{r}}_{edge}$ is facing "into" R, see [41, p. 248]. This case occurs if the system has a locally unstable fixed point, but a non-linearity that prevents an infinite deviation from the fixed point. Coming back to the dynamics in question, one would need to show that the network has a locally unstable fixed point at $(\mathrm{r_e}, \mathrm{r_i}) \approx (3\,\mathrm{Hz}, 13\,\mathrm{Hz})$, see A* in Figure 3. Several aspects come into play, making it a hard task to fit the full spiking network model onto the simplified equations 24 and 25. First, the choice of τ_e and τ_i in 24 and 25 has significant influence onto the stability of the system. However, a straightforward equivalent does not exist in the used spiking neuron model. It has been shown that in the case of slowly varying input $\tau_{e/i}$ of equation 24 and 25 are equal to the membrane constant τ_m of the LIF-neuron used in the network [42], see equation 7. A second problem is to choose a good estimate of the activation functions $\phi_{e/i}(\cdot)$. In the absence of noise in equation 7, the firing rate for a given constant total input J is

$$\phi(J) = \begin{cases} \frac{1}{-\tau_m ln(\frac{V_t - E_l - J\tau_m}{V_r - E_l - J\tau_m})} & \text{for } J\tau_m + E_l > V_t \\ 0 & \text{otherwise} \end{cases}. \tag{26}$$

If noise σ is present, according to [43] one can calculate the *mean* firing rate by

$$\phi(J) = \left[\sqrt{\pi}\tau_m \int_{x_-}^{x_+} dx e^{x^2} erfc(-x) \right]^{-1} \tag{27}$$

$$x_- = (V_r - E_l - J\tau_m)/\sigma \tag{28}$$

$$x_+ = (V_t - E_l - J\tau_m)/\sigma \tag{29}$$

where $erfc$ is the complementary error function. Figure 5 shows that both predictions are quite accurate in predicting the mean firing rate. However, one should note that the synaptic input within a spiking network carries an intrinsic randomness: since it is the sum of instantaneous increases in membrane voltage upon arriving spikes, one cannot simply describe it as a mean constant input J. Rather, if we assume that the arrival of spikes is approximately Poisson-distributed and the time constant of the membrane is small compared to the average interspike-interval, according to [43], one can describe the synaptic input from population A to population B as $J_{AB}(t) = \mu_{AB}(t) + \sigma_{AB} \cdot \zeta(t)$,

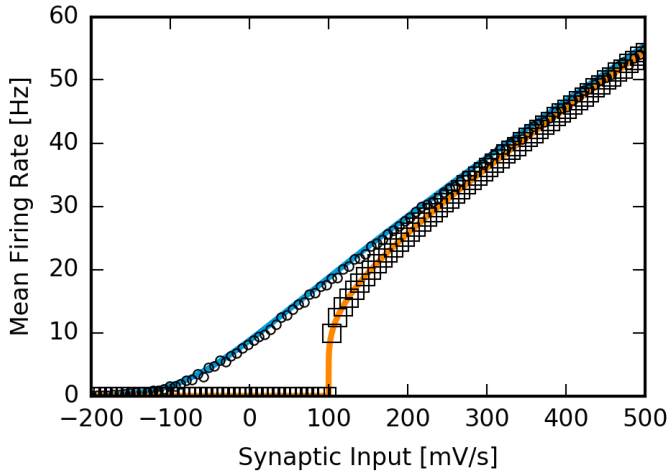

Figure 5: Comparison of mean firing rate of a LIF neuron without noise (squares) and with noise (circles, $\sigma = \sqrt{5}\,\mathrm{mV}$), averaged over 50 s. Red and blue curves are the corresponding analytic predictions, see equation 26 and 27.

where $\zeta(t)$ is zero-mean standard gaussian noise and

$$\mu_{AB} =< w_{AB} > \cdot < N_{in,AB} > \cdot < r_A > \tag{30}$$

$$\sigma_{AB} = \sqrt{\tau_m \cdot < w_{AB} >^2 \cdot < N_{in,AB} > \cdot < r_A >}\,. \tag{31}$$

$< \mathrm{w_{AB}} >$, $< \mathrm{N_{in,AB}} >$ and $< \mathrm{r_A} >$ denote the mean weight of a synapse connection population A with population B, the mean number of incoming connections at a neuron in population B and the mean firing rate in population A (which makes it necessary to assume changes within the firing rate to be slow enough for a quasi-stationary description of the activity). Since we can assume intrinsic and input noise to be uncorrelated, the total noise within a neuron of population B has a standard deviation of

$$\sigma_{tot.} = \sqrt{\sigma^2_{intr.} + \sum_A \sigma^2_{AB}}\,. \tag{32}$$

Apart from the correct description of $\phi_{e/i}$, a third problem is the analytic description of the STP that was present for recurrent excitatory connections in our network. In [34],

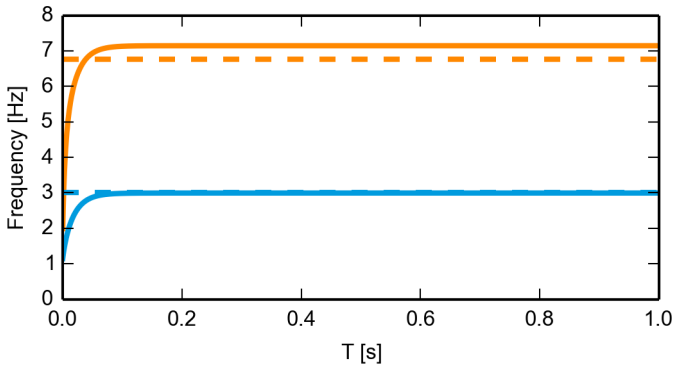

Figure 6: Dynamics of equations 24 (blue line) and 25 (red line). Dotted lines mark the mean frequencies that were present in the full spiking network. Excitatory: 3 Hz, Inhibitory: 6,768 Hz. 24 and 25 converged to 2.992 Hz and 7.144 Hz respectively.

the steady-state value of $x \cdot u$ for an input of constant rate r is given by

$$x_{st.}(r) = \frac{1 - \exp\left(-\frac{1}{r \cdot \tau_d}\right)}{1 - (1 - u_{st.}(r)) \cdot \exp\left(-\frac{1}{r \cdot \tau_d}\right)} \tag{33}$$

$$u_{st.}(r) = \frac{U}{1 - (1 - U)\exp\left(-\frac{1}{r \cdot \tau_f}\right)} \,. \tag{34}$$

When trying to find the fixed point of equations 24 and 25, one thus needs to incorporate the factor $x_{st.} \cdot u_{st.}$ by means of the previously described mean input and the contribution to the total variance of the membrane noise.

All these aspects taken together make it impossible to find an analytic expression for the fixed point of Equation 24 and 25. Running a simulation of 24 and 25, including all aforementioned approximations results in a stable configuration depicted in 6. For this simulation, we set the relevant parameters to their predefined values and, in addition, extracted the mean threshold of the excitatory population which was set by the non-diffusive homeostasis, see C/C* in Figure 3, yielding a threshold of $-56.963\,\mathrm{mV}$. The results are depicted in Figure 6. The system settled to a fixed point of $(r_{0,e}, r_{0,i}) = (2.992\,\mathrm{Hz}, 7.144\,\mathrm{Hz})$, which is quite close to $(3\,\mathrm{Hz}, 6.768\,\mathrm{Hz})$, being the mean excitatory and inhibitory firing rate between 100-750 s of the full simulation (i.e., during non-diffusive homeostasis). In principal, one could now further quantify the stability of the found fixed point by calculating the Jacobian matrix at $(r_{0,e}, r_{0,i})$. For the sake of the initial question though, namely the source of oscillation, it is sufficient at this point to restrict oneself to a preliminary result: Assuming validity of the described

rate-model, the recurrent network as such (without homeostasis) is stable under the given choice of parameters. Furthermore, on an empirical basis, the occurrence of oscillations appear to be rather dependent on the choice of homeostasis, since apart from the homeostatic mechanism itself, all parameters of the simulation were kept unchanged upon the transition after 750 s. Therefore, the following section further analyzes the dynamics underlying the diffusive homeostatic feedback.

3.2 Analysis of Oscillations under Dynamic Feedback

In this section, we discuss an analytic treatment of the dynamics underlying the diffusive homeostatic mechanism. The goal of this analysis was to predict the shape of the power spectrum shown in Figure 4. This gave insight into the relation between parameters of the model and the resulting preferred frequency and amplitude, allowing us to choose appropriate parameter values in order to reduce frequency and amplitude of the oscillations.

Both forms of homeostasis use excitatory firing thresholds as a means of adjusting the excitatory firing rate. Though having a relatively immediate impact on the firing rate of the particular neuron, the network as a whole reacts by means of a local disturbance of activity as well: It settles at a new fixed point of firing rates. Two questions are of importance in the context of feedback dynamics. First - obviously - how the relation between a local change of threshold and the new fixed point of the network can be described and second, whether the time scale of the network's response is of relevance with respect to other time scales involved in the feedback loop. Regarding the second question, Figure 7 suggests that the excitatory population activity follows the mean firing threshold in a quasi instantaneous fashion, at least in comparison with the overall time scale of the oscillating pattern. Thus, in a first attempt of understanding the occurrence of undesired oscillations, we presumed an immediate functional relationship $\mathbf{r}_e(t) = \mathbf{r}_e(\mathbf{V}_{t,e}(t))$, $\mathbf{r}_e$ and $\mathbf{V}_{t,e}$ representing the set of excitatory firing rates and thresholds, respectively.

Describing the neural activity as instantaneous firing rates raises the question how to describe the production of nitric oxide, since the outcome of equations (11) and (12) relies on sudden increases of Ca^{2+} concentration caused by spike events. Naively, one could replace the sum of Dirac functions in (11) by a continuous inflow $Ca^{2+}_{spike} r_i(t)$. If (12) was a linear homogeneous differential equation, this approximation would indeed allow for the correct calculation of a linear relation between mean firing rate and NO production. The cubic dependence on Ca^{2+} breaks this simplicity. In order to derive an approximate description, we denote two things: First, the target firing rate of 3 Hz

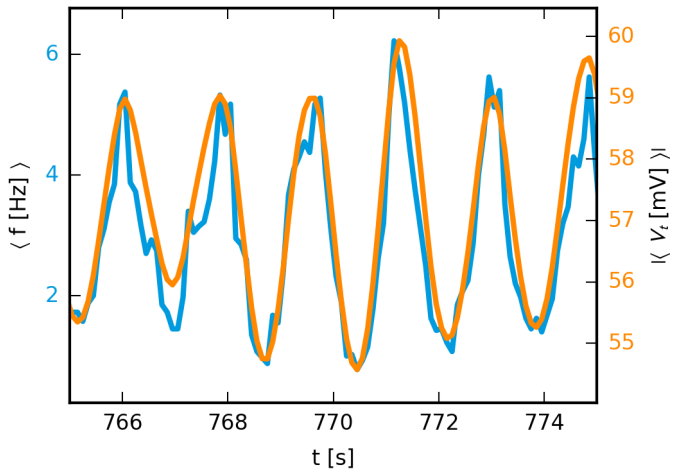

Figure 7: Time course of the mean firing rate (blue) and the mean firing threshold within the excitatory pool (red). Bin width for firing rate estimation was 0.1 s.

and the corresponding mean interspike interval of 0.33...s is large compared to the decay constant of calcium, $\tau_{Ca^{2+}} = 0.01\,\mathrm{s}$. Consequently, it is very unlikely that one spike event will fall into a region where the calcium concentration, decaying from the instant jump of the previous spike event, is still significantly larger than zero. As such, one can justify

$$\begin{aligned} {Ca^{2+}}^3(t) &= \left[Ca^{2+}_{spike} \sum_i \theta(t - t^i_{spike,i}) exp(-(t - t^i_{spike,j})/\tau_{Ca^{2+}}) \right]^3 \\ &\approx {Ca^{2+}_{spike}}^3 \sum_i \theta(t - t^i_{spike,i}) exp(-3(t - t^i_{spike,j})/\tau_{Ca^{2+}}) \end{aligned} \tag{35}$$

with $\theta(x)$ being the Heaviside step function. By the same argument

$$\frac{{Ca^{2+}}^3(t)}{{Ca^{2+}}^3(t) + 1} \approx \sum_i \theta(t - t^i_{spike}) \frac{exp(-3(t - t^i_{spike})/\tau_{Ca^{2+}})}{exp(-3(t - t^i_{spike})/\tau_{Ca^{2+}}) + \frac{1}{{Ca^{2+}_{spike}}^3}} \tag{36}$$

Therefore, the resulting rate of NO synthesis can be decomposed into a sum of time shifted responses onto a single kernel of calcium concentration as a result of a spike. for

a spike at $t_{spike} = 0$, the solution of (12) can be calculated by

$$\begin{aligned} nNOS(t) &= \frac{1}{\tau_{nNOS}} \int_{-\infty}^{t} dt' exp(-(t-t')/\tau_{nNOS}) \cdot \theta(t') \frac{exp(-3t'/\tau_{Ca^{2+}})}{exp(-3t'/\tau_{Ca^{2+}}) + \frac{1}{Ca_{spike}^{2+\ 3}}} \\ &= \frac{1}{\tau_{nNOS}} \int_{0}^{t} dt' exp(-(t-t')/\tau_{nNOS}) \cdot \frac{exp(-3t'/\tau_{Ca^{2+}})}{exp(-3t'/\tau_{Ca^{2+}}) + \frac{1}{Ca_{spike}^{2+\ 3}}} \ . \end{aligned} \tag{37}$$

The exact solution of this integral can be expressed in terms of the hyper-geometric function, making it rather impractical for any further analysis. Looking for further simplifications, we noted that τ_{nNOS} is ten-fold larger than $\tau_{Ca^{2+}}$. This discrepancy in decay times allows for the assumption that the impact of the calcium kernel onto $nNOS$ is practically instantaneous. Consequently, $nNOS(t)$ becomes

$$nNOS(t) = \frac{1}{\tau_{nNOS}} \theta(t) exp(-t/\tau_{nNOS}) \int_{0}^{\infty} dt' \frac{exp(-3t'/\tau_{Ca^{2+}})}{exp(-3t'/\tau_{Ca^{2+}}) + \frac{1}{Ca_{spike}^{2+\ 3}}} \ . \tag{38}$$

In this form, the integral has an easy-to-handle solution, which - with all spike events now included - results in

$$nNOS(t) = \frac{Ca_{spike}^{2+\ 3} \tau_{Ca^{2+}} ln(2)}{3\tau_{nNOS}} \sum_{i} \theta(t - t_{spike}^{i}) \exp(-(t - t_{spike}^{i})/\tau_{nNOS}) \ . \tag{39}$$

Figure 8 compares the approximation given by (39) to the full NO production model (equations (11) and (12)). Spikes were drawn from a Poisson process at a rate of 3 Hz. As predicted, the simplified model fits very well for sufficiently isolated spike events. For the rare event of two subsequent spikes appearing very close to each other, as seen in Figure 8 at approximately 4 seconds, one can observe a slightly smaller but acceptable agreement.

Returning to the question of how to describe NO synthesis in a simplified form, we note that according to equation (39), a single spike causes the release of NO by an amount of $\frac{Ca_{spike}^{2+\ 3} \tau_{Ca^{2+}} ln(2)}{3}$, which makes the mean rate of NO production over time simply $< nNOS > = < r > \cdot \frac{Ca_{spike}^{2+\ 3} \tau_{Ca^{2+}} ln(2)}{3}$. However, it is not sufficient to simply propose $nNOS_i(t) = r_i(t) \cdot \frac{Ca_{spike}^{2+\ 3} \tau_{Ca^{2+}} ln(2)}{3}$. A single cell fires in the range of 3 Hz, which is - at least on the time scale of the observed oscillations - not enough to assign an "instantaneous" firing rate.

To deal with this, we introduced an idealized picture of diffusive homeostasis, where diffusion across the tissue is instantaneous. This simplification results in a single level of NO-concentration for all neurons, only being modified over time by the sum of all

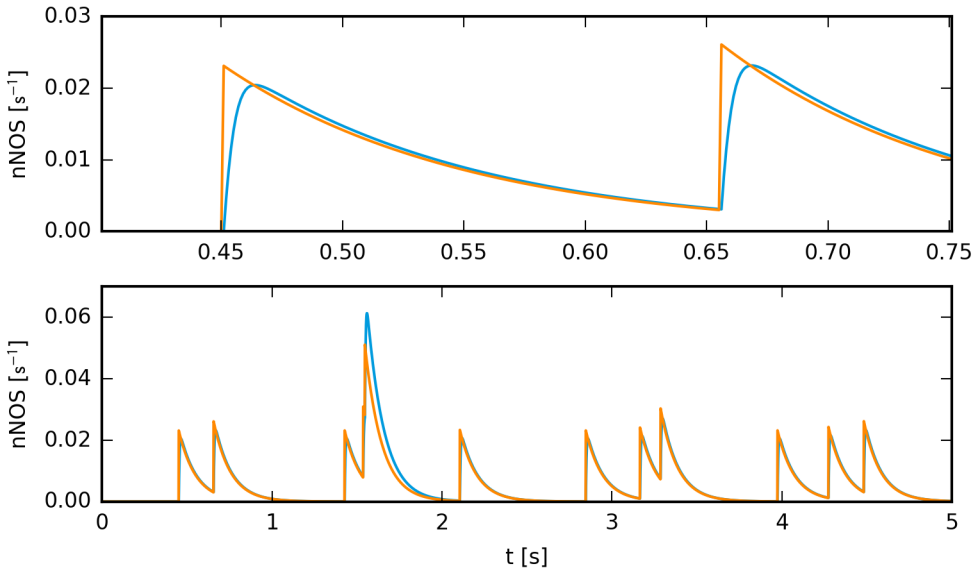

Figure 8: Time course of nNOS(t) with Poisson spiking at 3 Hz. The full simulation (blue, see equations (11),(12)) is well fitted by the simplified model (red, see equation (39)). Top axis is a closeup of the first spike event.

neurons' NO-syntheses $nNOS_{total}(t) \equiv \sum_i nNOS^i(t)$ and the decay term $-\lambda NO$. To account for the spread of NO, $nNOS_{total}$ must be divided by the area L^2 of the tissue. Furthermore, we introduce a random fluctuation term $\sigma_{NO}\xi(t)$ that accounts for local, momentary deviations from the mean. The idealized version of (13) then reads

$$\dot{NO}(t) = -\lambda NO + \frac{nNOS_{total}(t)}{L^2} + \sigma_{NO}\xi(t) \; . \tag{40}$$

The amount of noise in the system is a hard-to-predict quantity since it depends on the spatial structure on the diffusive lattice, giving neurons that are further separated less impact onto each other. We tried to estimate the noise level based on the same "instant spread"-simplification made in Equation (40) to describe the overall NO-dynamics. In the final result, this led to an underestimation of the total energy within the power spectrum. However, as long as we assume the noise in the system to be approximately white, noise level only acts as a global scaling factor of the shape of the power spectrum and was thus left open as a model fitting parameter.

From Equation (40) it is clear why we can now describe the *total* influx of NO as the sum of a mean and a random fluctuation: While spiking events on individual cells remain sufficiently separated to justify equation (39), the sum of all spike events from the excitatory population results in an effective Poisson process with a mean rate of

$3Hz \cdot N_{exc.} = 1200\,\text{Hz}$, given the assumption that cells are spiking weakly correlated. Furthermore, we argue that a total rate of 1200 Hz is sufficiently large to express this rate as a continuous function of time, $r_{total} = N_{exc.} \cdot r_{exc.pop.}(t)$, at least on the time scale of the oscillations to be studied (see Figure 7). We thus propose

$$nNOS_{total}(t) = r_{exc.pop.} \cdot N_{exc.} \frac{{Ca^{2+}_{spike}}^3 \tau_{Ca^{2+}} ln(2)}{3} \tag{41}$$

where $\frac{{Ca^{2+}_{spike}}^3 \tau_{Ca^{2+}} ln(2)}{3}$ is the integral from Equation (38).

As a next step, we wanted to simplify the dynamics of threshold adaption and its effect on the population rate. Corresponding to the reduction to a single variable $r_{exc.pop.}(t)$ for the mean excitatory activity in equation (41), we wanted to find an appropriate description containing only the mean threshold $V_{t,pop.}(t) =< V_t(t) >$. As stated earlier, Figure 7 suggests an immediate and approximately linear relation between excitatory population rate and the mean of thresholds within the excitatory population. Figure 9 shows a linear fit (being of the form $\alpha x + \beta$) of these two quantities plotted against each other. Apart from rarely appearing high values of $V_{t,pop.}$, we found a good fit to the linear model. We thus expressed the population rate by $r_{exc.pop.}(t) = r_{IP} + \alpha(V_{t,pop.}(t) - V_{t,0})$, where r_{IP} is given in table 3 as the mean excitatory target firing rate and $V_{t,0} \equiv (r_{IP} - \beta)/\alpha$ is the mean threshold corresponding to the target rate.

Combining these results in a set of equations, we find

$$\dot{NO}(t) = -\lambda NO + \frac{(r_{IP} + \alpha(V_{t,pop.}(t) - V_{t,0})) \cdot N_{exc.} \frac{{Ca^{2+}_{spike}}^3 \tau_{Ca^{2+}} ln(2)}{3}}{L^2} + \sigma_{NO}\xi(t) \tag{42}$$

$$\dot{V_{t,pop.}}(t) = \frac{NO - NO_0}{NO_0 \tau_{V_t}} \,. \tag{43}$$

Through the coordinate transformations

$$n \equiv NO - NO_0 \tag{44}$$

$$\theta \equiv V_{t,pop.}(t) - V_{t,0} \tag{45}$$

$$\tag{46}$$

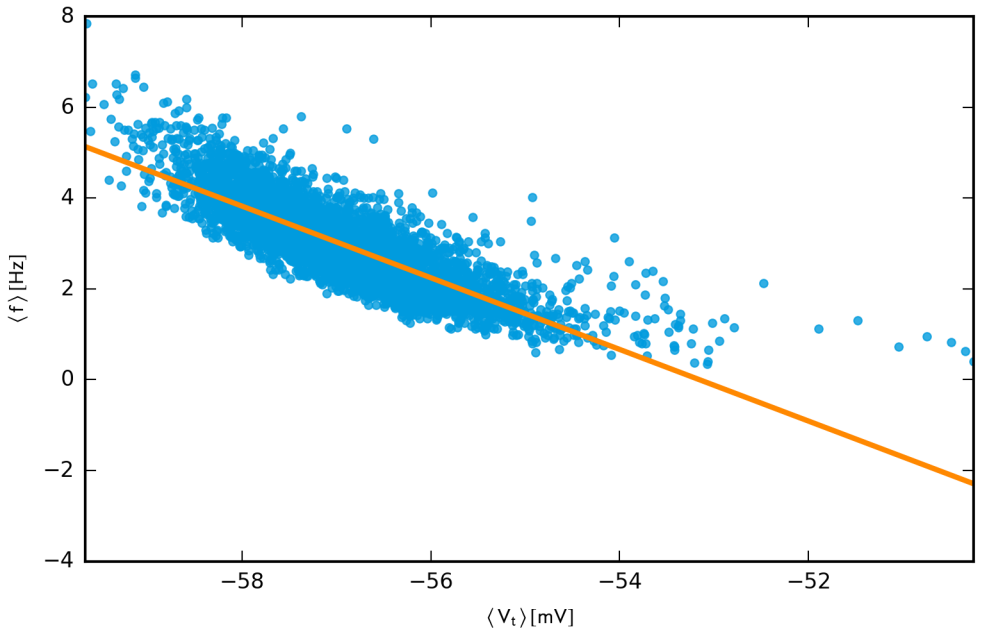

Figure 9: Linear fit of excitatory population activity and mean excitatory threshold. Slope α of the fit: $-0.789\,\mathrm{Hz/mV}$. Offset β: $-41.97\,\mathrm{Hz}$. Mean squared error: $\mathrm{R}^2 = 0.68$.

we can simplify the dynamical system:

$$\dot{n} = -\lambda n + \frac{\gamma \alpha N_{exc.}}{L^2}\theta + \sigma_{NO}\xi(t) \tag{47}$$

$$\dot{\theta} = \frac{1}{NO_0 \tau_{V_t}} n \tag{48}$$

where we have additionally used

$$\gamma \equiv \frac{{Ca^{2+}_{spike}}^3 \tau_{Ca^{2+}} ln(2)}{3} \tag{49}$$

$$NO_0 = \frac{nNOS_{total,0}}{\lambda L^2} \tag{50}$$

$$nNOS_{total,0} = r_{IP} \cdot N_{exc.} \cdot \gamma\ . \tag{51}$$

As stated in the beginning, we were interested in finding an analytic expression for the power spectrum of the mean excitatory threshold. Therefore we took the Fourier

transform of (47) and (48), yielding

$$i\omega f_n = -\lambda f_n + \frac{\gamma\alpha N_{exc.}}{L^2} f_\theta + \sigma_{NO} f_\xi \tag{52}$$

$$i\omega f_\theta = \frac{f_n}{NO_0 \tau_{V_t}} \tag{53}$$

$$\tag{54}$$

where $f_{(\cdot)}$ denotes the Fourier transform. We solved for f_θ which immediately gave us the power spectrum $P_\theta(\omega) \equiv |f_\theta(\omega)|^2$ of θ:

$$P_\theta(\omega) = \frac{\sigma_{NO}^2}{\omega^2 NO_0^2 \tau_{V_t}^2 \lambda^2 + \left(\omega^2 NO_0 \tau_{V_t} + \frac{\gamma\alpha N_{exc.}}{L^2}\right)^2} \tag{55}$$

Since we assumed the noise term ξ to be approximately white and gaussian noise with unit variance, its power spectrum is $|f_\xi|^2 = 1$.

Figure 10 shows the result of (55). Choosing noise amplitude to be the only free parameter of the model gave a rather unsatisfying result. Our approximation underestimated the amount of damping within the system (which controls the "peakiness" of the spectrum), as well as predicting a slightly smaller preferred amplitude. While the broadness of the spectrum is mostly controlled by the damping term $-\lambda$, the preferred amplitude is controlled by $\frac{\gamma\alpha N_{exc.}}{L^2}$ and $\frac{1}{NO_0\tau_{V_t}}$. Since the latter term was taken unaltered from the original system (apart from a shift in phase space), we added $-\lambda$ and α as free fitting parameters and managed to get a very good fit to the simulation data, see Figure 10. The fact that the value for α that was determined by means of the linear fit in Figure 9 leads to an underestimation of the preferred frequency can be partially explained by the linear regression, which overestimates the importance of a number of high-threshold-outliers. This leads to a shallower slope than what would be appropriate for the "working point" of oscillatory behavior. Another possible explanation could be that "instant spread" is only an approximation. Rather, one could picture the nitrous oxide just to fill a fraction of the available space on a short time scale by replacing L^2 by a smaller area. This leads to a stronger local increase of concentration, which eventually leads to faster oscillations. In either case, since these parameters appear as a fraction α/L^2 in (55), both parameters have the same effect onto the shape of the power spectrum.

In the context of the presented power spectra, reducing oscillations meant to reduce height and frequency of the peak of the spectrum. We managed to do so by increasing the time constant $\tau_{\mathrm{V_t}}$, as shown in Figure 11. Moreover, by choosing σ_{NO}, λ and α in

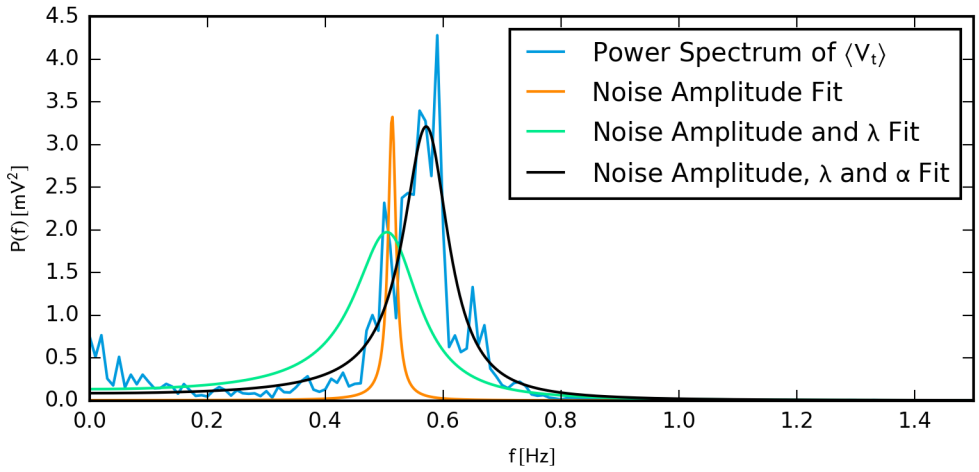

Figure 10: Power Spectrum of $\langle V_t \rangle$ (blue) and analytic predictions based on Equation (55). Red curve was fitted by tweaking only the overall amplitude σ_{NO} in (55) ($\alpha = -0.789\,\mathrm{Hz/mV}$, as in Figure 9). Green curve is a fit achieved by adjusting σ_{NO} and λ in (55) ($\lambda = 0.845\,\mathrm{s}^{-1}$). Black curve was fitted by means of σ_{NO}, λ and α ($\lambda = 0.592\,\mathrm{s}^{-1}$, $\alpha = -0.989\,\mathrm{Hz/mV}$).

accordance to the fit shown in Figure 10 (black curve), Equation (55) provides a good prediction for the position and height of the peak. For proper comparison, we smoothed the curve of the simulation data in plot (A) of Figure 11 by a window of $[-5, 5]$ data points, since the maximum of the power spectrum of simulation data is likely to overshoot the analytic prediction due to random fluctuations. To reduce oscillations as much as possible we eventually settled at a 1000-fold increased time constant, $\tau_{V_t} = 2500\,\mathrm{s}$. Even given the slowness of threshold adaption, homeostasis still managed to keep excitatory network activity in the desired range, as shown in Figure 12. Despite a slight regularity of the time course of NO-concentration, no oscillating activity occurs. We took this setting as a basis for further analysis of network activity.

3.3 Properties of Network Activity

After the elimination of oscillatory activity in the network, we further investigated the features of neural activity, in particular of the excitatory population, since it was exposed to homeostasis. This includes statistics of spike timing, as well as of heterogeneous firing rates among the network.

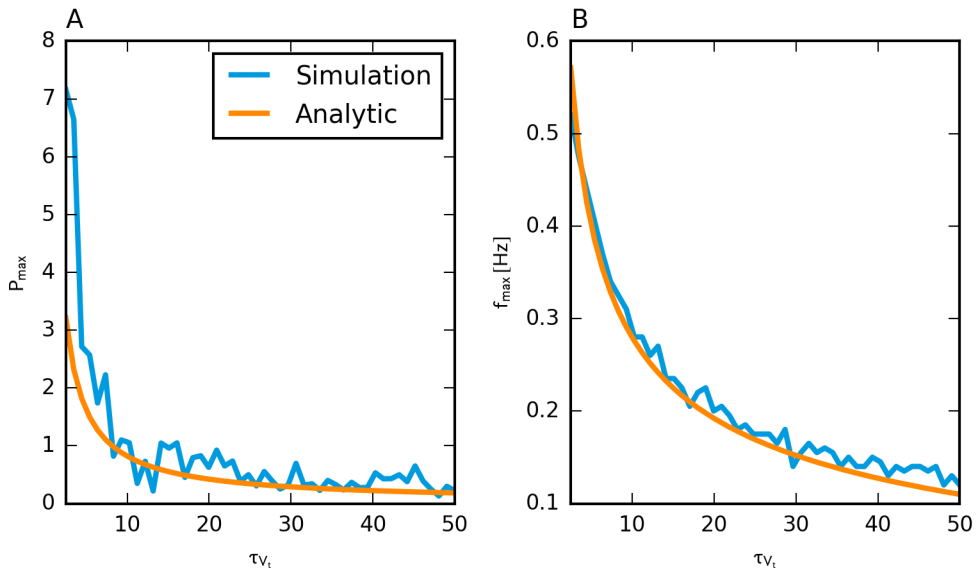

Figure 11: A: Maximum of the spectrum-peak (see Figure 10). A smoothing window of $[-5, 5]$ data points around the maximum was used to reduce overestimation of the maximum due to random fluctuations. Blue line corresponds to Equation (55), fit values taken from black curve in Figure 10. B: Position of the peak on the frequency axis. Analytic prediction was acquired according to (A).

3.3.1 Spike-Train Statistics

Balanced networks of inhibitory and excitatory populations of spiking LIF-neurons are known to show highly random, uncorrelated spiking behavior under sparse connectivity with a relatively high per-synapse connection strength [44,45]. This kind of asynchronous regular state is characterized by a population firing rate showing no regularities over time, though maintaining an overall stable level of activity. This regularity was shown to be achievable in the previous section after slowing down the rate of homeostatic adaption. On the level of single cells, interspike intervals should be random, approximately following the statistics of a Poisson process. Figure 13 shows the distribution of interspike intervals (ISIs) and the distribution of coefficients of variation (CV $\equiv \sigma/\mu$), taken over the set of excitatory and inhibitory neurons, respectively. However, in order to provide comparability between the ISI distributions in the diffusive/non-diffusive case, we restricted the statistics of ISIs to neurons whose mean firing rate fall into a window with a width of 1 Hz and a certain mean (see legend in Figure 13). Apparently, an approximately exponential distribution of ISIs is preserved for diffusive homeostasis (represented by straight lines in a log-plot), which is characteristic for Poisson processes [8, p. 27]. For perfect poissonian spiking, the CV should give a value of 1. CVs that are smaller

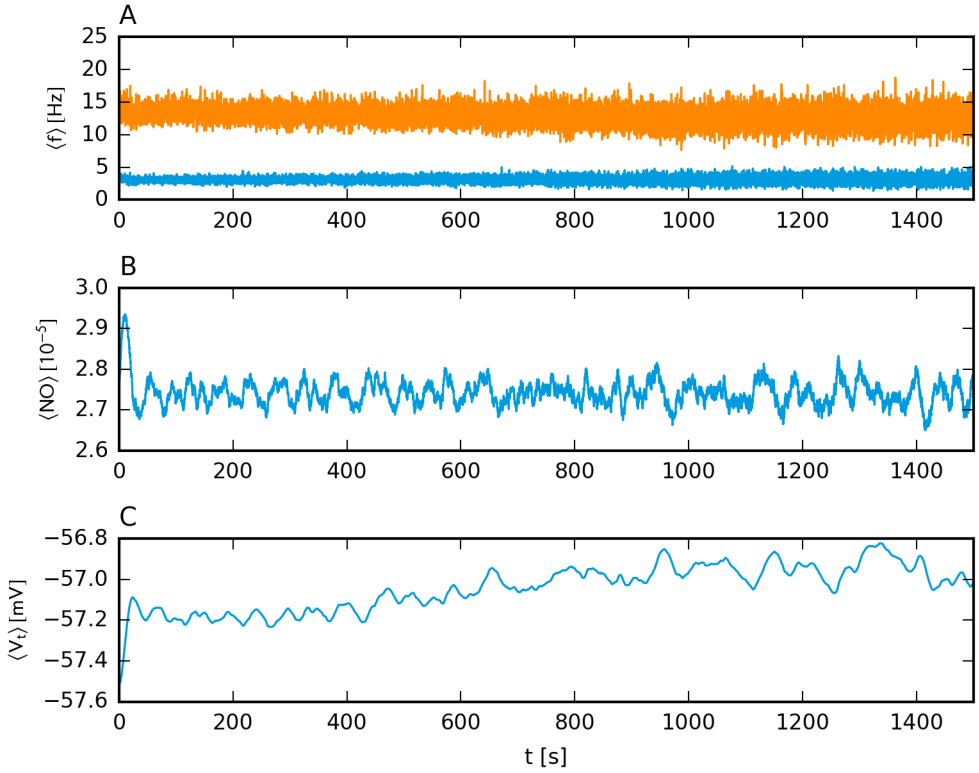

Figure 12: A: Excitatory (blue) and and inhibitory (red) population rate, being controlled by diffusive homeostasis over the full simulation time. B,C: Mean NO-concentration over excitatory sites and mean excitatory threshold.

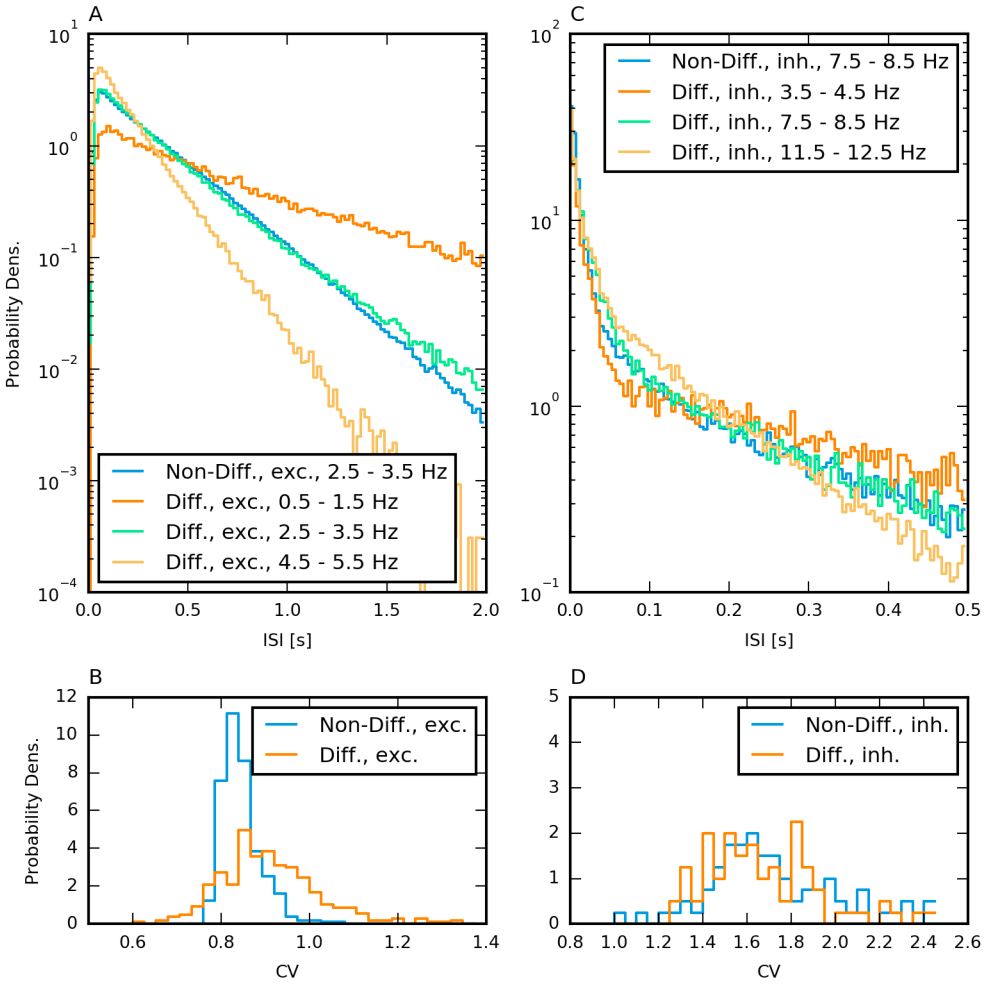

Figure 13: A/C: Distribution of interspike intervals of excitatory/inhibitory neurons for diffusive and non-diffusive homeostasis, measured over 1000 s. Only neurons with a mean firing rate in a certain range (see legend) were included into statistics to prevent overlap of different firing rates (except for non-diffusive homeostasis and excitatory neurons, all being very close to 3 Hz). Black lines are fits of exponential functions. B/D: Distribution of coefficients of variation. Each sample represents the CV of one excitatory/inhibitory neuron.

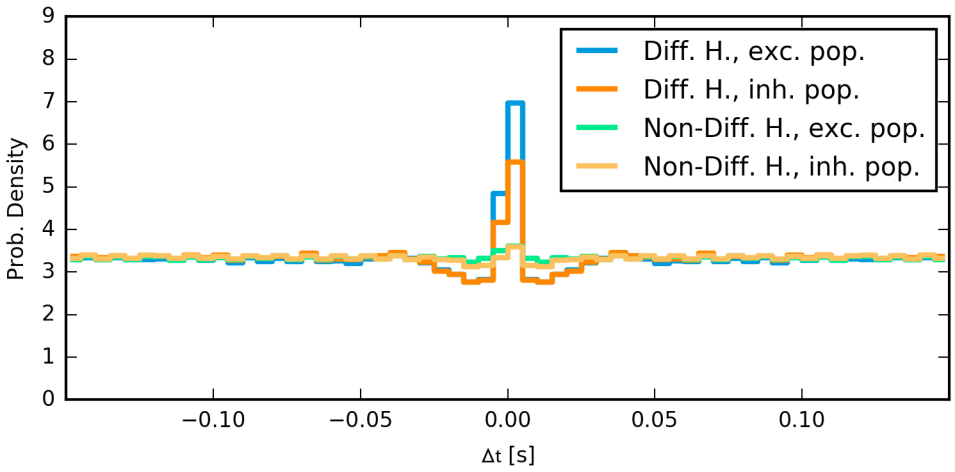

Figure 14: Mean of cross correlation over all pairs of neurons in the respective neuron-group. Significantly higher correlation can be found in both groups for diffusive homeostasis. Spike data was taken from $1400 - 1500\,\mathrm{s}$ of the simulation.

or larger, as seen in Figure 13 B/D, indicate a tendency towards greater regularity or bunching, respectively. This observation is presumably due to the statistics of ISIs close to zero: Interestingly, while excitatory neurons have an under-representation of short ISIs, the opposite is the case for inhibitory neurons. These types of behavior of LIF-models have been shown to depend on the CV of input the neuron receives: A smaller signal-to-noise-ratio (larger CV) of neural input leads to a larger CV of ISIs for the output and an over-representation of small intervals [46]. This relation fits nicely into our set of network parameters: Inhibitory neurons receive stronger recurrent inhibitory input ($-60\,\mathrm{mV}$ in total) compared to excitatory neurons ($-12\,\mathrm{mV}$). This lowers the signal-to-noise ratio for the inputs of inhibitory neurons, leading to the aforementioned statistical differences. Still, one can observe a dominant exponential component for both excitatory and inhibitory neurons.

As an additional possibility of spike-train analysis, we looked at potential correlations across neurons within both populations. To do so, we calculated cross-correlations for all possible neuron-pairings within a population, excluding auto-correlations. Figure 14 shows the mean cross-correlation taken over all these pairs. Surprisingly, we found a significant increase in correlation across neurons for diffusive homeostasis. When speculating about the root of this discrepancy one could consider two possibilities: Either, it is an immediate consequence of diffusive homeostasis, or it is indirectly related through other mechanisms present within the network. Regarding the first, it is certainly true that some amount of information about the activity of one neuron is transferred to

another one in its neighborhood via diffusion. However, due to the time scale of the homeostatic adaption, the response to fluctuations in the diffusive signal is on the order of seconds, while correlations in Figure 14 are taking place within milliseconds. Thus, we concluded that a *direct* link between homeostatic signaling and increased correlations can be regarded as implausible and that it must be an effect based on topological differences within the network. We investigate these in Section 3.4.

In summary, we found that diffusive homeostasis does not interfere with the poisson-like spiking statistics observed on a single-cell level, but leads to an increased correlation across the neural population.

3.3.2 Distribution of Firing Rates

Achieving a broad distribution of firing rates among neurons was the core motivation for the implementation of diffusive homeostasis. Figure 15 shows a first result, comparing both homeostatic mechanisms. As expected, non-diffusive homeostasis leads to a sharp distribution of firing rates at 3 Hz. Diffusive homeostasis indeed results in a much broader distribution of mean firing rates. As mentioned in the introduction, a large number of experimental studies have found that distributions of firing rates are not only broadly distributed but well described by a log-normal distribution, which has a non-zero third moment or skewness. By definition, the logarithm of the random variable in question is thus again normally distributed. To check for this property we plotted the the distribution of decadic logarithms of firing rates in Figure 15 (B). In (A), we found a skewness of $v_{\mathrm{Diff}} = 0.765$, in (B) $v_{\mathrm{Diff,log}} = -0.488$. Though this told us that the distribution is "more symmetric" on a logarithmic scale, it should rather be seen as being neither strictly normally or log-normally distributed. In contrast, inhibitory cells showed a much clearer distinction: A skewness of $v_{\mathrm{Diff}} = 1.522$ in regular space and $v_{\mathrm{Diff,log}} = -0.147$ in log-space.

Despite of fluctuations within the firing rate on small time scales due to the inherent nature of - approximately - random spike generation, we wanted to know how strongly firing rates of single excitatory cells fluctuate over longer timescales of multiple seconds. This question is not only of relevance with respect to the "stiffness" of homeostasis, but also relates to the plot in Figure 15: If firing rates fluctuate too much during the period over which means were calculated, the resulting distribution might be narrower than what one could expect from a distribution of "momentary" rates. A constant "rate" of an approximately randomly spiking neuron means that the dependence of fluctuations of rates onto the width of the averaging window should be identical to a homogeneous poisson process of the same total mean firing rate. As bin sizes increase, possible long-

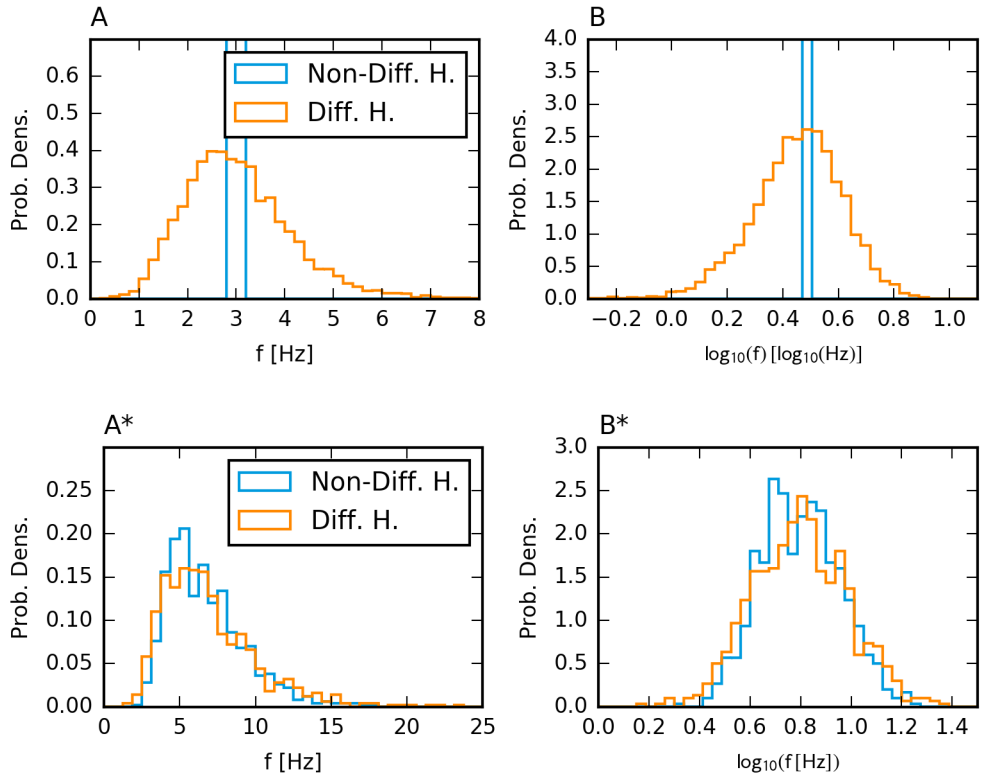

Figure 15: Histograms of mean firing rates over the excitatory/inhibitory population in regular (A/A*) and logarithmic space (B/B*). For diffusive homeostasis ($D = 1000\,\mu m^2 s^{-1}$), the distribution was generated from 10 simulation runs, 1 simulation was used for non-diffusive homeostasis. Mean firing rates were calculated from spikes within $t = 1000 - 1500\,s$.

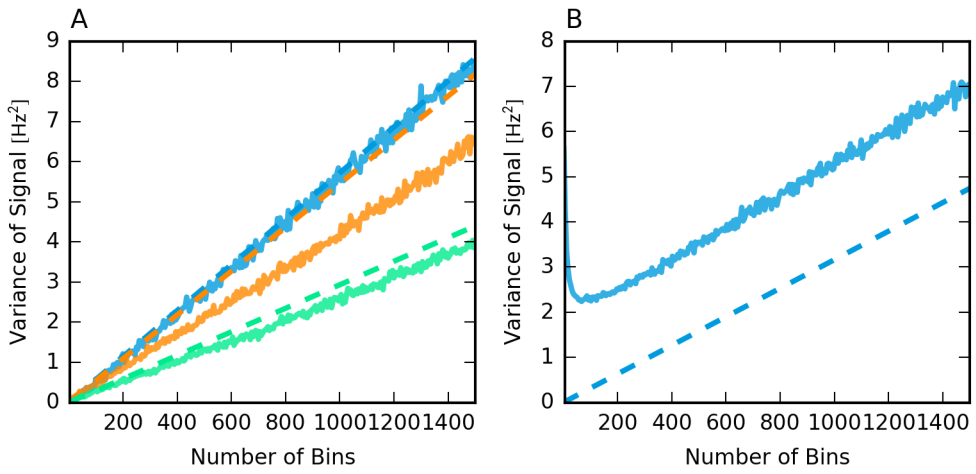

Figure 16: A: Relation between Variance of the frequency signal (acquired by binning spikes) and the number of bins within the given time range of $1000 - 1500\,\mathrm{s}$, taken from three randomly picked excitatory neurons. B: Same procedure as in (A) for a randomly chosen excitatory neuron, but time range was $0 - 1500\,\mathrm{s}$, which includes the initial phase of non-diffusive homeostasis. In both plots, dashed lines are the expected curve of a homogeneous poisson process of the same mean rate.

term fluctuations of firing rates can then be identified as deviations from the variance one would expect from a homogeneous process. We tested this in Figure 16. (A) was taken from $1000 - 1500\,\mathrm{s}$, which is well inside the phase of diffusive homeostasis. As one can see, the statistics of the three representative neurons are well fitted by the predictions for homogeneous poisson processes with the same mean rate, being a straight line given by $\mathrm{var} = \mathrm{f_{mean}} \cdot \mathrm{n_{bins}}/\mathrm{T_{total}}$, though slight deviations can be seen as a different factor of proportionality. (B) acts as an illustration showing a counterexample: Here, we included the entire time span of the simulation, including the transition between non-diffusive and diffusive homeostasis. For almost all of the neurons, this will cause a transition of firing rate between 3 Hz and a new rate different from 3 Hz. This inhomogeneity is represented by the increasing positive relative deviation from the dashed line for small number of bins (i.e., large bin widths), even increasing again for a very few number of bins. We therefore concluded that diffusive homeostasis manages to retain firing rates on a constant level, not only population-wise but on a single-cell level as well. In particular, plastic modifications across the network due to STDP and synaptic growth/pruning - which were always acting for all the simulation results presented so far - appeared to be compensated for.

As an additional test, we applied external Poisson input for $\mathrm{t} \geq 300\,\mathrm{s}$ to two excitatory subgroups to see whether changes in the firing rate of these subgroups is leveled

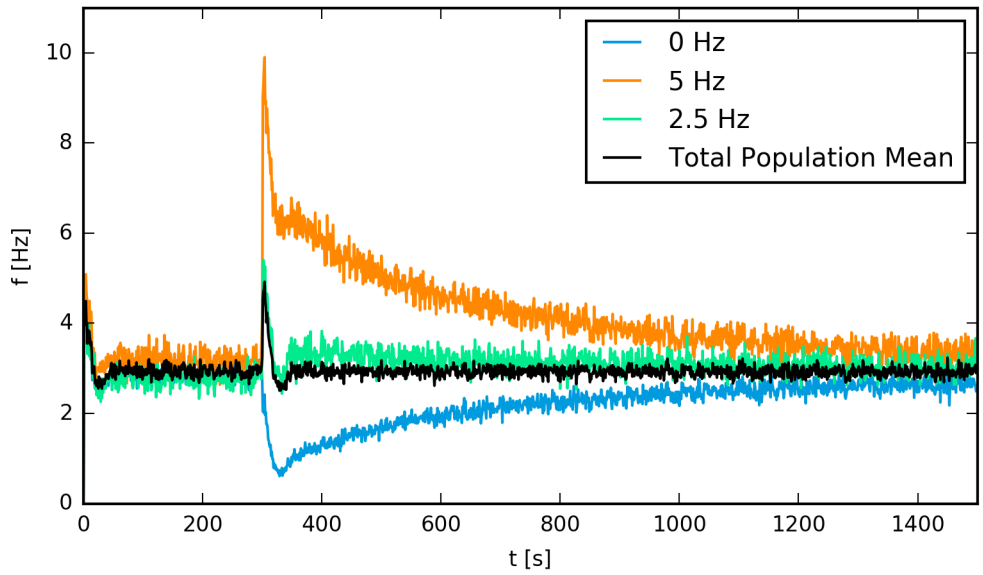

Figure 17: Excitatory population firing rate of subgroups subject to external poisson input for $t \geq 300\,s$. Red and green subgroups consist of 100 randomly picked excitatory neurons each. The remaining 300 neurons (blue) received no external input.

out by homeostasis or retained. Members of these subgroups were picked randomly and independent of their position. As shown in Figure 17, differences among subgroups caused by different input signal strengths are gradually eliminated by the homeostatic mechanism.

Sweeney et al. found that diffusive homeostasis maintains broadness of firing rates across a wide range of diffusion constants but rapidly approaching zero for small values [17, p. 6]. We were able to reproduce this result, see Figure 18 (A). Homeostasis reaches a point of saturation, where faster diffusion has no effect on the heterogeneity of firing rates. To further quantify this dependence, we also investigated the influence of the diffusion constant onto the distribution's skewness, shown in Figure 18 (B). Compared to the standard deviation, we see a similar but not as clear trend with a drop for very small diffusion constants, even occasionally resulting in a left-skewed distribution (negative D-values).

A naturally emerging question when altering the diffusion constant is how the firing rate behaves in the absolute limit of infinitely fast diffusion. In fact, simulation-wise this case is quite easy to simulate: One simply has to feed all NO-sources into a single scalar variable of NO concentration. In particular, this will provide the same NO readout for all excitatory neurons, which means that all excitatory thresholds change at the same rate all the time, only shifting their initial random distribution. Figure 19 shows the

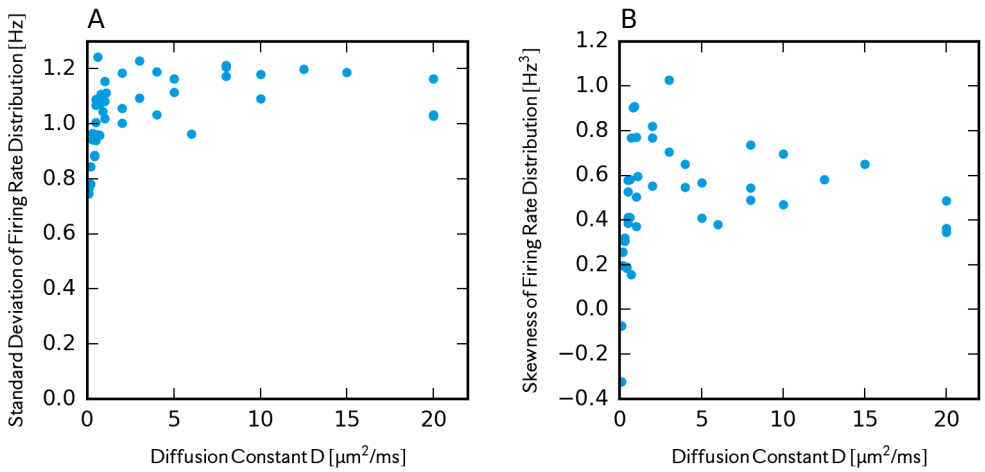

Figure 18: Standard deviation (A) and skewness (B) of firing rate distribution of excitatory neurons (Neumann boundary conditions).

distribution for this special limiting case. The standard deviation for the excitatory population was $\sigma_{\text{inst}} = 1.79\,\text{Hz}$ and the skewness $\text{v}_{\text{inst}} = 1.51$ ($\text{v}_{\text{inst,log}} = -0.52$), which makes the asymmetry slightly more pronounced than in Figure 15.

Summing up the results of this section, we can state that stable network activity can be achieved in the LIF-SORN with diffusive homeostasis while producing a broad distribution of firing rates within the excitatory population. We found that this ensemble of activity is maintained on a single cell level, each cell spiking with approximately poissonian statistics at a constant mean rate. The broadness of distribution could be maintained at a relatively constant level over a wide range of diffusion rates. However, we did not find a distribution as right skewed and heavy tailed as reported by Sweeney et al. and numerous experimental studies.

3.4 Network Topology

So far, we have only analyzed network activity, whereas in this section we present results that relate to features of synaptic topology. Since the SORN we used for all simulations only included plastic mechanisms affecting recurrent excitatory connections, these were the subject of our investigations. Moreover, in contrast to the previous section, we did not explicitly aim for the emergence of a *new* feature of synaptic topology, but rather sought to recover properties that had been found in earlier versions of the LIF-SORN.

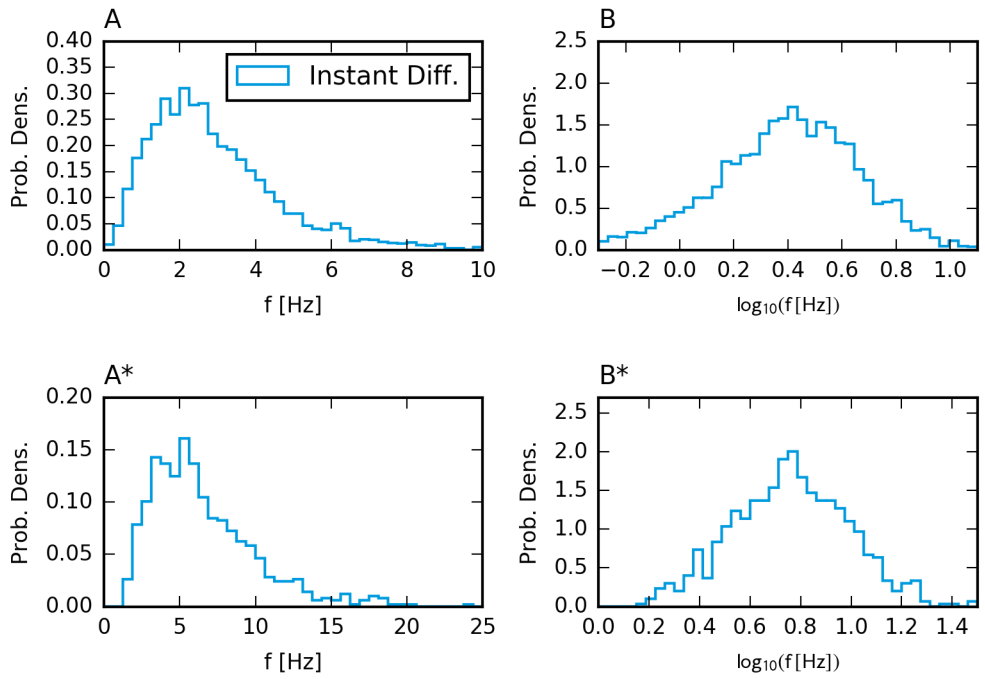

Figure 19: Distribution of firing rates for instantaneous diffusion for excitatory (A,B) and inhibitory (A*,B*) population. Data was taken from 10 simulations and $t = 1000 - 1500\,s$.

3.4.1 Excitatory Connection Fraction

In the previous version of the LIF-SORN, initializing the network with zero recurrent excitatory connections led to a monotonically increasing but saturating excitatory-to-excitatory connection fraction (CF). The growth rate was tuned such that the terminal CF settled at 10%, see [25, p. 8]. Omitting the distance dependence of connection probability for synaptic growth led to a slightly higher connection fraction. To compare these previous results to the diffusive case, we ran a full simulation under diffusive homeostasis, including the growth phase by setting the target concentration to an appropriate value that was determined in a previous simulation with non-diffusive homeostasis. The resulting time course of CF is depicted in Figure 20. Diffusive homeostasis caused the CF to slightly overshoot its final fraction in the growth phase. To understand this kind of behavior, we recalled the two mechanisms that directly determine changes within the connection fraction, namely synaptic growth and pruning. The average change of connection fraction is simply proportional to the difference between newly created synapses and those that were removed. Though fluctuating, the synaptic growth rate was kept at a constant level of 920 synapses/second. In consequence, any differences in Figure 20 must originate in different pruning rates. Figure 21 shows the mean and standard de-

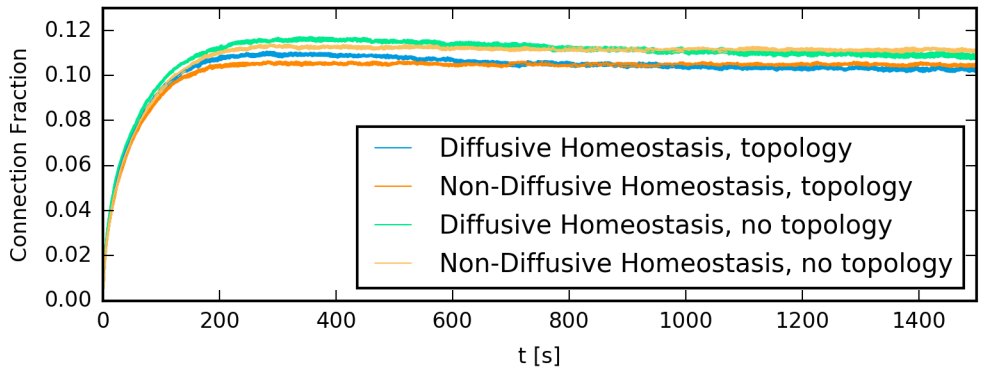

Figure 20: Connection fractions of recurrent excitatory synapses. Simulation protocols include all four possible combinations of diffusive/non-diffusive homeostasis and distance-dependent/non-distance-dependent synaptic growth, each variant retained for the entire simulation time. Data from 10 trials, linewidth represents standard error.

viation of weight changes due to STDP between two normalization steps. Non-diffusive homeostasis has a higher mean as well as a broader distribution of weight fluctuations throughout the beginning of the simulation. However, the difference of mean changes is orders of magnitude smaller than the width of fluctuations. Thus, while it might seem counter-intuitive that a higher positive mean weight change comes with a smaller chance of synaptic survival, we attribute the main cause of overshooting in Figure 20 to the increased fluctuation of weights, since it raises the chance of going below the pruning threshold within a given time interval. Apart from reproducing the desired connection fraction, previous versions of the LIF-SORN showed an over-representation of bidirectional connections compared to a random graph with equal connectivity [25]. This experimentally observed feature required the presence of a distance dependent connection probability, as described in section 2.1. The absence of this breaking of spatial homogeneity even led to an under-representation of bidirectional connections, which is known to be an effect of STDP in recurrent networks [7]. As shown in Figure 22, the separation between simulations with and without a spatial connection profile is retained.

3.4.2 Distribution of Synaptic Weights

A well-studied property of neural networks is the distribution of synaptic weights. Experimental studies in hippocampus and cortical regions suggest heavy-tailed log-normal-like distribution of synaptic efficacies [28, 47–49]. Theoretical models are mainly based on a combination of multiplicative and additive weight dynamics [49, 50], which is in line with our implementation of multiplicative normalization and additive STDP. Figure 23

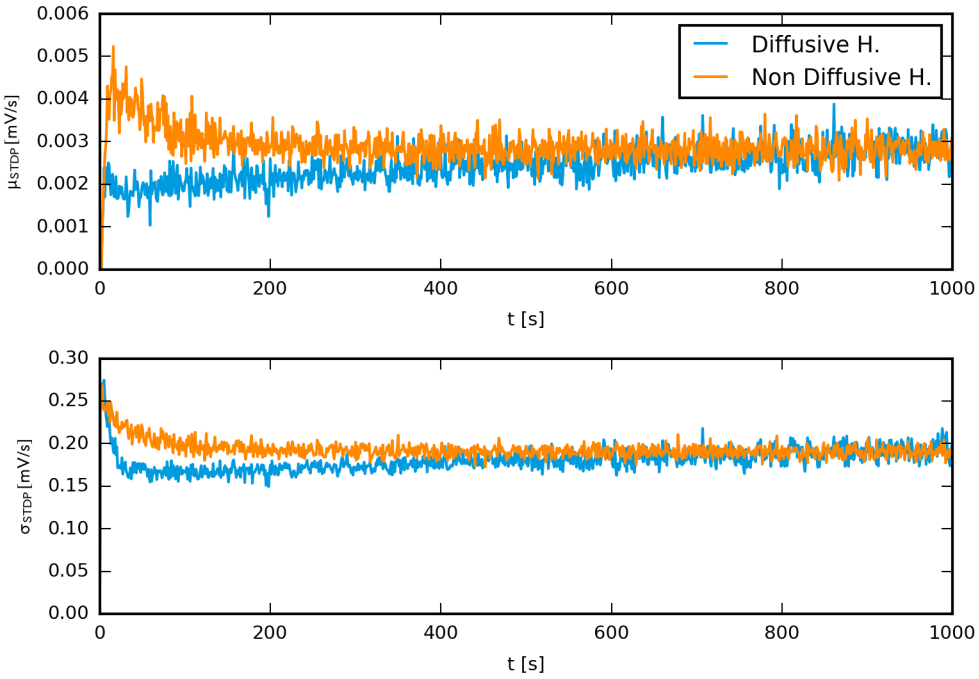

Figure 21: Top: Mean change of synaptic weights (growth and pruning excluded) between two normalization steps. Bottom: Standard deviation for the same data. Both curves correspond to those in Figure 20 with the same color.

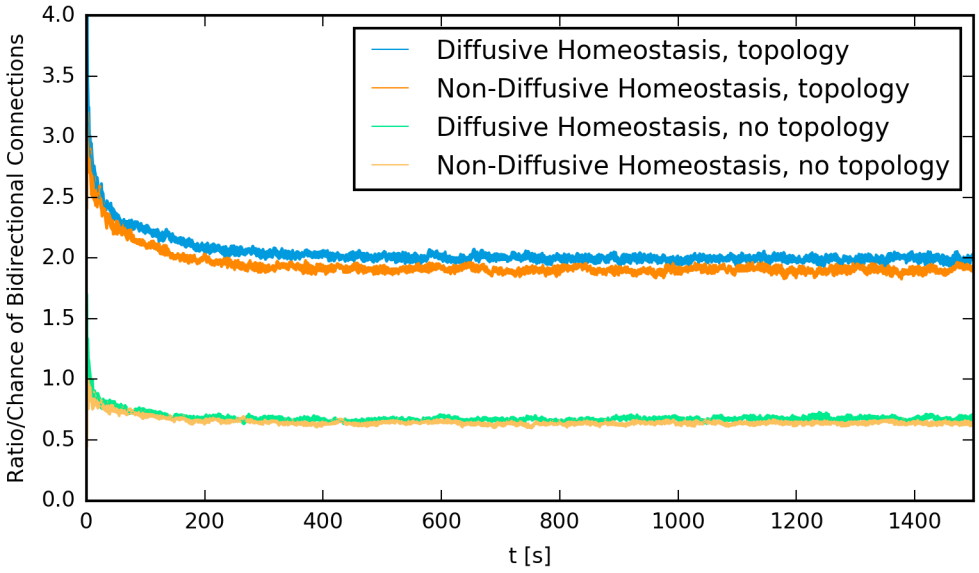

Figure 22: Fraction of bidirectional connections normalized over the expected fraction for a random graph with equal total connection fraction. Data from 10 trials, linewidth represents standard error.

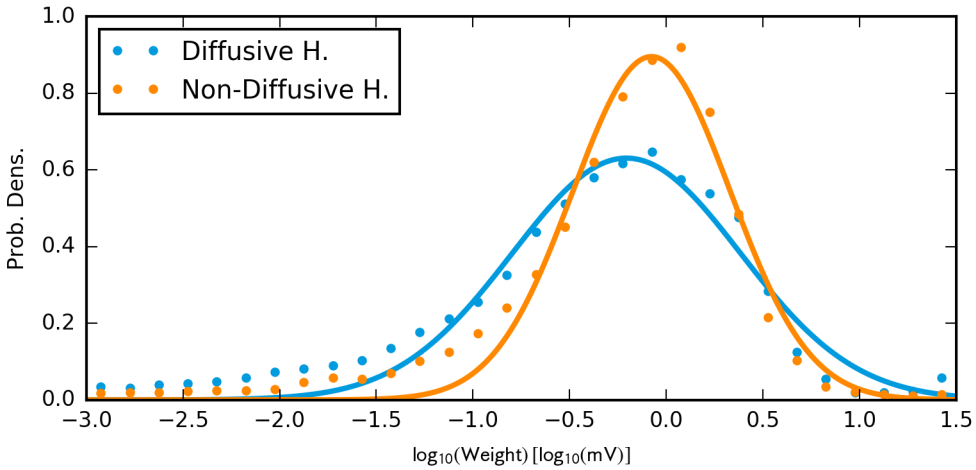

Figure 23: Distribution of decadic logarithm of excitatory synaptic weights at t = 1500 s for diffusive and non-diffusive homeostasis (both with distance-dependent connectivity). Gaussian fits returned $\mu_{\text{diff}} = -0.172\,\log_{10}(\text{mV})$, $\mu_{\text{non-diff}} = -0.087\,\log_{10}(\text{mV})$, $\sigma_{\text{diff}} = 0.643\,\log_{10}(\text{mV})$ and $\sigma_{\text{non-diff}} = 0.418\,\log_{10}(\text{mV})$.

compares the resulting distributions. We found that we can retain a log-normal-like distribution in combination with diffusive homeostasis. A slightly larger variance can be observed. A possible explanation refers back to our observations in Figure 21: Regarding STDP as a random process, a broader distribution of weights can be explained by a smaller potentiating effect and a decreased variance of STDP-fluctuations, which is both the case for diffusive homeostasis in the beginning of the simulation. Still, it seems unlikely that a possible effect of these differences is still present at t = 1500 s.

3.4.3 Synaptic Lifetimes

Synaptic lifetimes have been shown to approximately follow a power law distribution in earlier versions of LIF-SORN and binary SORN [25, 26]. This feature was preserved under diffusive homeostasis, as shown in Figure 24. The resulting slopes are within previously reported values of $\approx -5/3$ [25]. To get an approximative explanation for the observed slope in the region of small lifetimes, we note that short synaptic lifetimes are most likely coming from synapses whose weights did not reach large values compared to the initial weight. In this regime of small weights, the effect of multiplicative normalization is small compared to additive STDP. Therefore, small weights are determined by additive quasi-random (due to their weak coupling to the postsynaptic neuron) fluctuations, which, as a very simple approximation, can be described as a Brownian motion with certain standard deviation σ. The first hitting time of this Brownian motion is

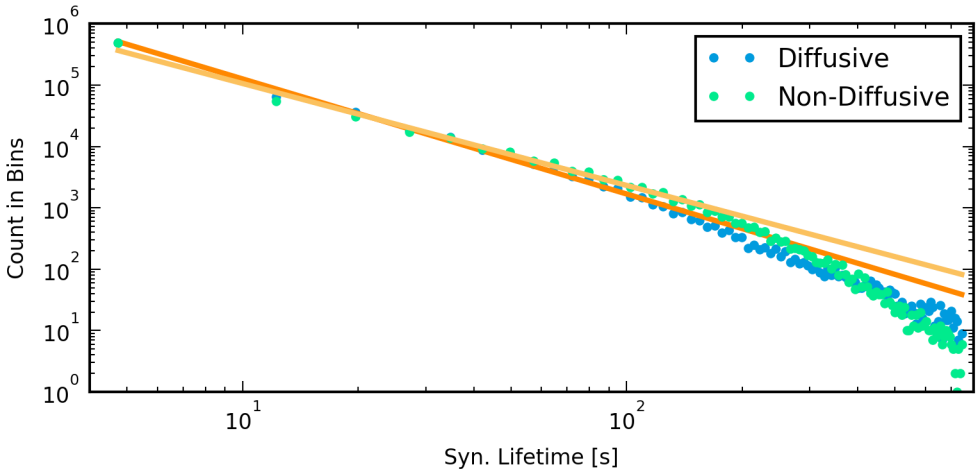

Figure 24: Distribution of recurrent excitatory synaptic lifetimes. Linear fits ignoring falloff for large synaptic lifetimes resulted in a slope of -1.871 for diffusive homeostasis and -1.676 for non-diffusive homeostasis.

described by a Lévy distribution:

$$p(t, w_0, w_{prune}) = \frac{|w_0 - w_{prune}|}{\sqrt{2\pi\sigma t^3}} exp\left(\frac{(w_0 - w_{prune})^2}{2\sigma t}\right) \tag{56}$$

For larger t, the dominating term is $t^{-3/2}$, which roughly resembles the power-law exponents found in Figure 24.

3.4.4 Mean outgoing Weights

Since we only implemented synaptic normalization for the sum of *ingoing* weights, the total or average strength of *outgoing* connections may vary from cell to cell. In a sense, the strength of outgoing connections per neuron can be regarded as a measure of how "influential" a neuron's activity is with respect to other neurons in the network. Effenberger et al. have shown in computational studies that these "driver neurons" form highly active and interconnected subnetworks [51], an observation that is backed up by experimental studies [52, 53]. Figure 25 shows that diffusive homeostasis allows for the emergence of a small group of highly influential neurons, which reproduces the findings in [51]. A comparison of statistics generated with shuffled versions of the weight matrices illustrates that above-chance exceptionally strong outgoing weights were indeed present. Furthermore, we noted that the difference between shuffled matrices corresponding to non-diffusive and diffusive homeostasis is in line with our observation from Figure 23, which indicated a broader distribution of weights for diffusive homeostasis.

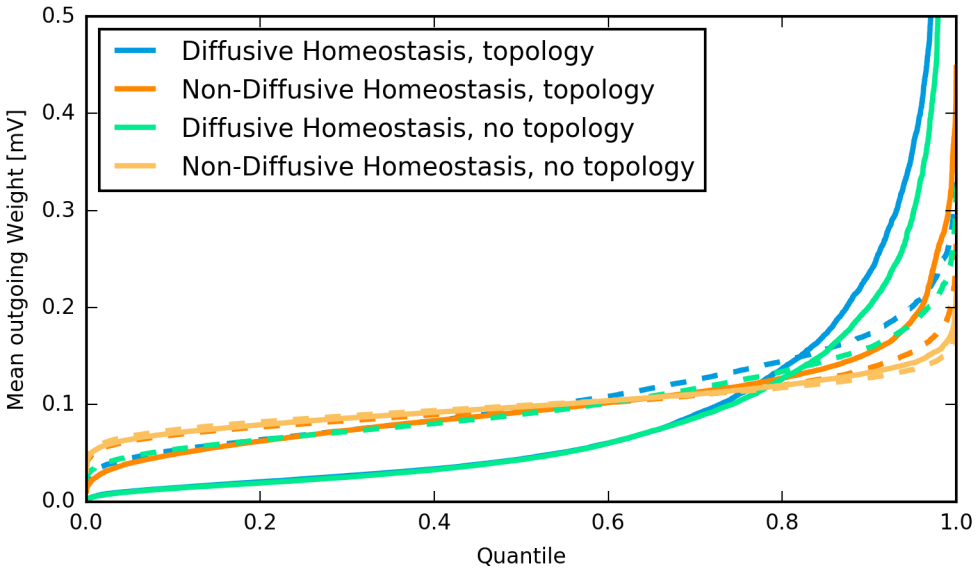

Figure 25: Mean of outgoing weights of excitatory neurons in order sorted by magnitude. Dashed lines are means obtained by randomly shuffling synaptic weights. Data was taken from 25 weight matrices per line, representing weights within $t = 1000 - 1500\,s$.

In contrast to our model, Effenberger et al. identified the presence of inhibitory STDP as a necessary mechanism for the development of this feature. On a deeper explanatory level, the authors argue that inhibitory STDP is indirectly involved: It weakens inhibitory currents for some neurons, which cause these neurons to have more above-average firing rates. In turn, synapses between highly active presynaptic cells and postsynaptic neurons with lower activity are known to be subject to long-term potentiation [54, 55]. With these causal relations in mind, we can argue that diffusive homeostasis effectively embodies the same functional role as inhibitory STDP in [51] by allowing for the presence of excitatory cells with above-average activity. We tested this relationship by plotting the mean outgoing weights against the average firing rate, see Figure 26. A strong heterogeneity of firing rates allows for the development of few strong synapses, while the distribution of mean weights resulting from a narrow distribution is limited to a smaller range. We also tested the case of instant diffusion. Though firing rates span across a similar range, mean weights do not reach as high values as in the case of diffusion at a finite rate. Furthermore, it is interesting to note that on a logarithmic weight scale, we found a roughly linear relationship. Figure 26 only depicts data from simulations including a distance dependent connection profile, since removing this topology did not result in noticeable differences.

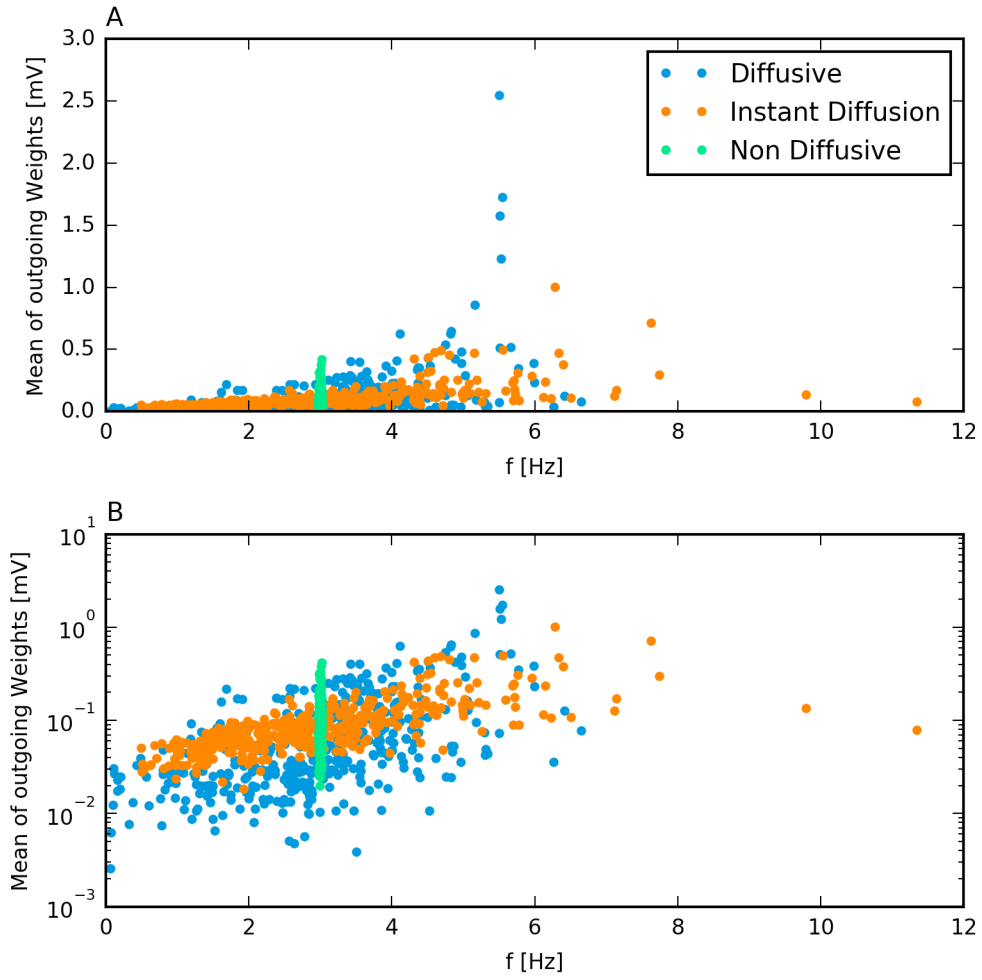

Figure 26: Mean of outgoing excitatory weights at $t = 1500\,s$ plotted against mean presynaptic firing rate (averaged over $t = 700 - 1000\,s$) in regular (A) and logarithmic space (B). Each plot corresponds to a presynaptic excitatory cell.

4 Further Analysis of the Firing Rate Distribution

On a preliminary level, the results of section 3.3.2 were positive with respect to our goal of achieving a broad and skewed firing rate distribution. Following this, we tried to further gain insight into the actual shape of the resulting distribution.

4.1 Review of a Dynamic Mean-Field Model

Sweeney et al. attempted to predict the shape of the firing rate distribution by means of a simplified mean-field approximation of diffusion [17]. The main simplification within homeostatic feedback was the replacement of Equation 14 by

$$\dot{V_t^i}(t) = \frac{1}{\tau_{HIP}} \left((1-\alpha) \frac{\phi_i - \phi_0}{\phi_i} + \alpha \frac{\langle \phi \rangle - \phi_0}{\langle \phi \rangle} \right) . \tag{57}$$

$\alpha \, \epsilon \, [0, 1]$ thereby acted as a parameter that determines the "mixture" between single-neuron-homeostasis ($\alpha = 0$) and the limit of quasi instantaneous spreading of the diffusive signal across the population ($\alpha = 1$). ϕ_i and $\langle \phi \rangle$ represent individual firing rates and their overall mean.

Furthermore, the spiking recurrent network was replaced by a set of non-interacting non-spiking neurons, whose individual mean firing rates were calculated by

$$\phi_i(\mu_i, \sigma_i, V_t^i) = \left[\sqrt{\pi} \tau_m \int_{x_-}^{x_+} dx e^{x^2} erfc(-x) \right]^{-1} \tag{58}$$

$$x_- = (V_r - E_l - \mu_i \tau_m)/\sigma_i \tag{59}$$

$$x_+ = (V_t^i - E_l - \mu_i \tau_m)/\sigma_i \tag{60}$$

which is the same formula we used in (27). Furthermore, in accordance to [43], mean and standard deviation of the inputs were calculated by Sweeney et al. as

$$\nu = \langle \phi \rangle = \frac{\sum \phi_i}{N} \tag{61}$$

$$\mu_i = J_i C_i \nu \tau \tag{62}$$

$$\sigma_i = J_i \sqrt{C_i \nu \tau} \tag{63}$$

where ν is the mean population firing rate, ϕ_i the individual firing rate of neuron i, μ_i, σ_i and V_t^i its synaptic input mean and standard deviation and intrinsic firing threshold respectively and J_i, C_i and τ the neuron's mean synaptic efficacy, number of incoming neurons and the membrane time constant. Synaptic efficacy and number of incoming neurons were drawn randomly to match the statistics of the actual network topology.

Self consistency was achieved by iterating through equations (58) and (61) - (61) until the desired precision of convergence is reached.

The authors claimed that this model reproduces results of the full network, in particular that the steady-state firing rate distribution spreads out due to a larger diffusion constant (or a larger α, respectively).

We tested this dynamic mean-field model by simulating a similar population, but used an interacting population of neurons of the same size as in the previous simulations (400 excitatory, 80 inhibitory neurons). This allowed us to directly use a weight matrix acquired by means of a simulation of the full plastic network, taken from the network after 1500 s (i.E., the "stable" phase). Individual values for μ_i and σ_i were then calculated according to (62) and (63). Note however that in this case the mean (input) firing rate ν also takes different values ν_i for each neuron.

Instead of directly iterating through equations (58) and (61) - (63) - as done in [17] - to fulfill self-consistency, we described the dynamics of the neurons' rates r_i through a continuous dynamic equation

$$\frac{dr_i}{dt} = \frac{1}{\tau_m}\left(-r_i + \phi_i(\mu_i(\nu), \sigma_i(\nu), \theta_i)\right) \tag{64}$$

where τ_m is the membrane time constant. Equation (61) had to be rewritten accordingly:

$$\nu_i = \langle r \rangle_{presyn.,i} \equiv \frac{\sum_{\exists syn.j \to i} r_j}{N_{presyn.,i}} \tag{65}$$

In addition, we included the modulation of weights by STP through a rate-dependent prefactor by combining Equation (5) and (6) into rate-based equations and solving for their steady state:

$$x_0 \cdot u_0 = \frac{1 + r_{total,i}\tau_f}{1/U + r_{total,i}(\tau_d + \tau_f) + r_{total,i}^2 \tau_d \tau_f} \tag{66}$$

where $r_{total,i}$ is the rate of all combined spikes arriving at neuron i.

Figure 27 depicts the resulting dynamics of excitatory rates and thresholds for $\alpha = \{0.4, 0.8, 0.9, 1.0\}$. Apparently, except for the limiting case of $\alpha = 1$, all rates approach the same target rate of 3 Hz and thresholds move towards the same configuration for either choice of α. A significant difference only exists within the transient dynamics leading to the steady state. Roughly speaking, a smaller value of α leads to a faster relaxation. These findings led us to the conclusion that, apart from the special case $\alpha = 1$, which is the equivalent to "instantaneous" diffusion, a mean-field model describing the diffusive signal as a mixture of individual activity and all neurons is not suitable

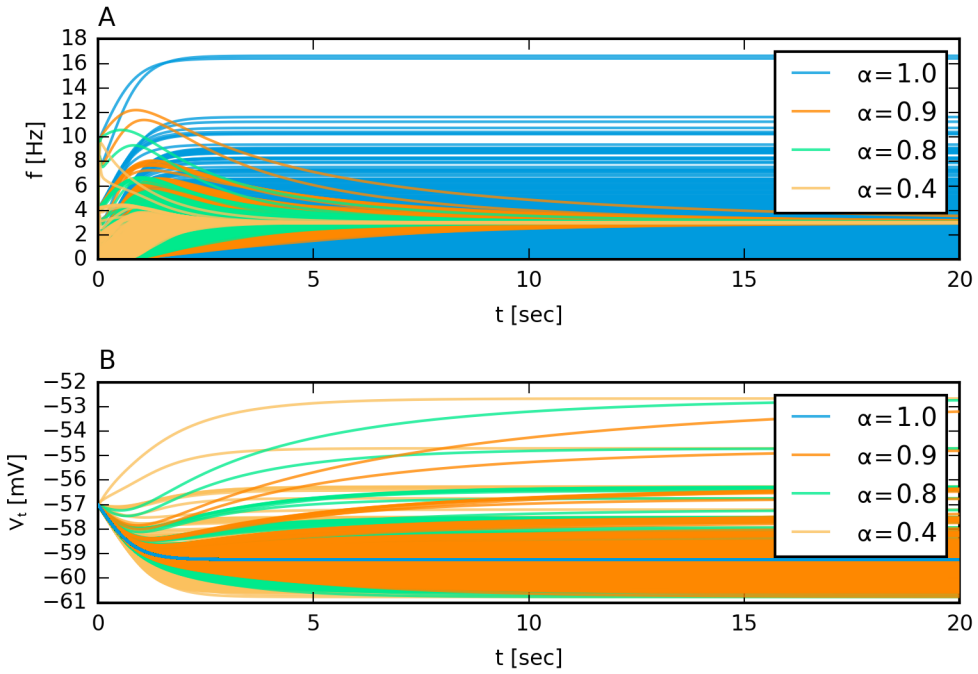

Figure 27: Dynamics of rates (A) and thresholds (B) of excitatory population of 400 Neurons and different values of α (see equations (64) and (57)).

for explaining the existence of stable heterogeneous distributions of rates for a broad range of diffusion constants. We did not intent to debase the validity of results of the mean-field model of Sweeney et al. However, by analyzing Equation 57, we could show that the steady-state solution of this simplified model will result in the same firing rate ϕ_0 for all neurons, given any value of α except $\alpha = 1$. This can be seen by setting the left hand side of Equation (57) to 0 (which is necessarily the case in the steady state) and rearranging the equation:

$$(\alpha - 1)\frac{\phi_i - \phi_0}{\phi_i} = \alpha\frac{\langle\phi\rangle - \phi_0}{\langle\phi\rangle} \tag{67}$$

The right term of the equation is the same for all neurons. Since the left term is monotonically increasing as a function of ϕ_i as long as $\alpha < 1$, only one specific solution $\phi_i = \Phi$ for all i exists that equals the given term on the right. Furthermore, this implies $\langle\phi\rangle = \Phi$. Thus,

$$(\alpha - 1)\frac{\Phi - \phi_0}{\Phi} = \alpha\frac{\Phi - \phi_0}{\Phi} \tag{68}$$

which is only fulfilled for $\Phi = \phi_0$.

Moreover, one can argue that this result also implies a fixed distribution of thresholds

in the steady state, independent of α: Given the result above, one finds

$$\phi(\mu_i(\nu), \sigma_i(\nu), V_t^i) = \phi_0 \tag{69}$$

$$\mu_i = J_i C_i \phi_0 \tau \tag{70}$$

$$\sigma_i = J_i \sqrt{C_i \phi_0 \tau} \tag{71}$$

$$\rightarrow V_t^i = \phi^{-1}(J_i C_i \phi_0 \tau, J_i \sqrt{C_i \phi_0 \tau}, \phi_0) \tag{72}$$

which implies that the set of V_t^i only depends on the given network topology.

4.2 Equilibrium in the full Diffusive Model

Since the previous section has shown that the simplified model in [17] has problems in maintaining a broad distribution of firing rates, turning to a more general formulation of the problem seemed reasonable.

We did so by recalling that Equation (13) describes the full dynamics of the diffusive neurotransmitter. Furthermore, equation (42) represents a simplification by means of two assumptions, namely the disregard of the diffusive term and the simplification of the process of NO-generation to a simple relation $\mathrm{nNOS_i} = \gamma \cdot \mathrm{r_i}$, $\mathrm{r_i}$ representing a neuron's rate and γ being defined by Equation (49). In this section we discuss the implications of an "in-between" description, only applying the second simplification, but retaining the diffusive term:

$$\frac{dNO}{dt}(\mathbf{x}, t) = -\lambda NO + D\nabla^2 NO + \sum_i \delta^2(\mathbf{x} - \mathbf{x}_{neur,i}) \cdot \gamma \cdot r_i \tag{73}$$

As in the previous section, we ask for the steady-state distribution of rates. Thus as a first step, we had to solve

$$(\lambda - D\nabla^2)NO = \sum_i \delta^2(\mathbf{x} - \mathbf{x}_{neur,i}) \cdot \gamma \cdot r_i \tag{74}$$

for $\{\mathrm{r_i}\}$, such that

$$NO(\mathbf{x}_{neur,i}) = NO_0 \ , \ \forall i \ . \tag{75}$$

At this point, we were aware of the fact that these equations completely neglect fluctuations of NO-synthesis due to spiking. However, given the very slow adaption of thresholds, which are responsible for changes of firing rates, we argued that noise can be neglected in the sense that $\{\mathrm{r_i}\}$ represents the set of mean firing rates whose resulting spike-train-induced NO-synthesis *on average* fulfills (74) and (75).

Equation (74) can be rewritten as

$$\left(\nabla^2 + \left(i\sqrt{\frac{\lambda}{D}}\right)^2\right) NO = \sum_i \delta^2(\mathbf{x} - \mathbf{x}_{neur,i}) \cdot \frac{-\gamma \cdot r_i}{D} \tag{76}$$

which is a two-dimensional Helmholtz equation with a superposition of rescaled Dirac functions. Thus, the solution of NO is composed of a superposition of shifted and scaled versions of the Green's function of the differential operator on the left hand side of the equation. For each delta function $\delta^2(\mathbf{x} - \mathbf{x}_i)$, the solution is

$$NO_i(\mathbf{x}) = \frac{r_i \gamma}{2\pi D} K_0\left(|\mathbf{x} - \mathbf{x}_{neur,i}|\sqrt{\frac{\lambda}{D}}\right) \equiv r_i \cdot \psi_{point}(|\mathbf{x} - \mathbf{x}_{neur,i}|) \tag{77}$$

where K_0 is the zeroth modified Bessel function of the second kind [56]. This solution reveals a fundamental problem of modeling the sources of NO-production as point sources: the fact that $K_0(x)$ diverges to infinity for $x \to 0$. It is merely due to the finite density of the numeric grid used for the simulation of the diffusion that allows for a finite target value of concentration. Note that this problem only occurs in the two- or three-dimensional version of the differential equation, whereas in one dimension, the fundamental solution can be expressed as an exponential function with respect to the distance to the origin, resulting in a well-defined finite value at $x = 0$.

Generally speaking, no matter how the actual shape of the numeric solution in the equilibrium at a constant production rate looks like, it must be of the form

$$NO_i(\mathbf{x}) = r_i \cdot \psi(d(\mathbf{x}_{neur,i}, \mathbf{x})) \tag{78}$$

$$d(\mathbf{x}, \mathbf{y}) \equiv |\mathbf{x} - \mathbf{y}| \, . \tag{79}$$

The full solution is then

$$NO(\mathbf{x}) = \sum_i NO_i(\mathbf{x}) \, . \tag{80}$$

By defining

$$\psi_{ij} \equiv \psi_{ij} \equiv \psi(d(\mathbf{x}_{neur,i}, \mathbf{x}_{neur,i})) \tag{81}$$

we could express the condition (75) as

$$\sum_j \psi_{ij} \cdot r_j = NO_0 \tag{82}$$

or, as an operator

$$\hat{\psi}\mathbf{r} = NO_0\mathbf{n} \tag{83}$$

$$\mathbf{n} \equiv (1, 1, ..., 1) \ . \tag{84}$$

The problem of finding the steady-state solution of the homeostatic constraint thus reduced to inverting $\hat{\psi}$:

$$\mathbf{r} = NO_0\hat{\psi}^{-1}\mathbf{n} \tag{85}$$

Still, to acquire any prediction from this model, we had to find a modified, non-diverging version of $\psi(\mathrm{d}(\mathbf{x}_{\mathrm{neur,i}}, \mathbf{x}))$ that retains the shape given by (77) for larger distances but approaches the correct "numeric error"-value at the origin, determined by the spacing of the numeric grid. We "solved" this problem by the following expression:

$$\psi_{approx.} \equiv \frac{1}{\left(\frac{1}{\psi_0^{\varepsilon}} + \frac{1}{\psi_{point}^{\varepsilon}}\right)^{\frac{1}{\varepsilon}}} \tag{86}$$

where ε determines the "smoothness" of transition between ψ and the cutoff value ψ_0. We chose $\varepsilon = 10$ for all further calculations. To find an expression for ψ_0, we took the simple approach of interpreting this value as a mean of the analytic solution across the area covered by the corresponding grid cell. As an additional simplification, we substituted the necessary integration over the square grid cell by a circular area of equal size around the source. This calculation yielded

$$\psi_0 = \gamma \frac{1 - h\sqrt{\frac{\lambda}{\pi D}} K_1\left(h\sqrt{\frac{\lambda}{\pi D}}\right)}{h^2\lambda} \tag{87}$$

where h is the spatial resolution of the grid cells. Figure 28 shows a comparison between the numerically calculated solution and the expression given by 86. As expected, the approximation fitted very well for nonzero values. The value at the critical point in the origin was slightly underestimated by (87), but nonetheless fitted well into the overall shape. Thus, we took this approximation as a basis for further calculations of the interaction-matrix $\hat{\psi}$.

By simply calculating all matrix elements of $\hat{\psi}$ by means of Equation (81), one would neglect the finite boundaries of the system, which would cause neurons close to the edge to "bleed" into empty space. This in turn would cause the solution of (83) to contain an over-representation of high firing rates, since close-to-the-edge neurons would need to compensate for their lack of neighbors. Thus, we had to account for the boundary

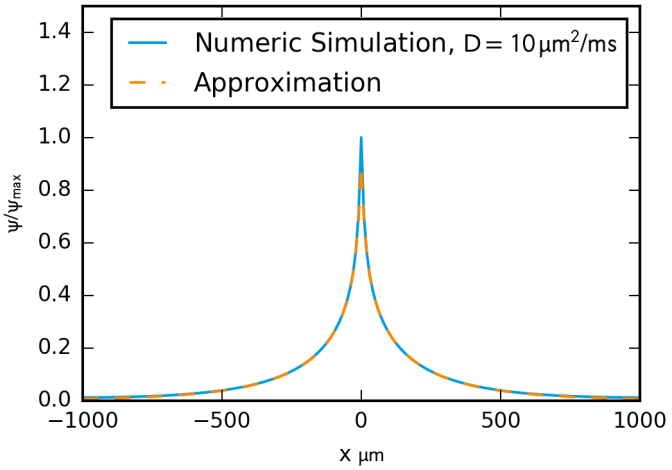

Figure 28: Numerical steady-state solution of Equation (76) (blue, h = 10 μm) and its approximation (dashed) given by (86). The numerical simulation was carried out on a 2d-grid and the curve represents a cut through the origin in x-direction.

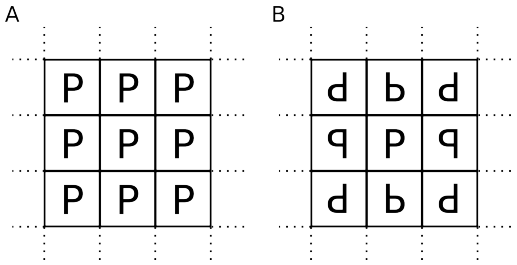

Figure 29: Sketch for patches of copied (and mirrored) positions for periodic (A) and Neumann (B) boundary conditions.

conditions used in the network simulation. As described in section 2, we simulated the network mostly with Neumann boundary conditions as well as periodic boundaries. Both types can be modeled by extending the neurons' population through spatially shifted and mirrored versions of the base population (see Figure 29):

- Periodic boundary conditions are induced by copies of the neurons' positions shifted by $L \cdot (n_x, n_y)$, $n_x, n_y \in \mathbb{Z}$.
- Zero flux through the boundaries can be achieved by copied positions being shifted by $L \cdot (n_x, n_y)$, $n_x, n_y \in \mathbb{Z}$ *and* mirrored in $x(y)$-direction if $n_x(n_y)$ is odd.

Therefore, the entries of the operator for periodic boundary conditions $\hat{\psi}_{per.}$ could be

calculated by

$$\psi_{ij,per.} = \sum_{n_x,n_y\in\mathbb{Z}} \psi_{approx.}(d(\mathbf{x}_{neur,i}, \mathbf{x}_{neur,i} + L\cdot(n_x,n_y))) \ . \tag{88}$$

For the Neumann boundary condition, one finds

$$\psi_{ij,neum.} = \sum_{n_x,n_y\in\mathbb{Z}} \psi_{approx.}\left(d(\mathbf{x}_{neur,i}, M(\mathbf{x}_{neur,i}) + L\cdot(n_x,n_y))\right) \tag{89}$$

$$M(\mathbf{x}) \equiv \begin{pmatrix} (-1)^{n_x} & 0 \\ 0 & (-1)^{n_y} \end{pmatrix} \mathbf{x} + L\cdot(mod(|n_x|,2), mod(|n_y|,2)) \ . \tag{90}$$

Note that the shift was applied to the second position. Theoretically, n_x,n_y is iterated over all integers and in this case it is irrelevant whether to shift the first or the second position. For our calculations, we obviously had to limit the amount of elements of the sum such that copies that are shifted further away can be neglected. For the sake of performance, the number of terms in the sum was adjusted to suffice the given diffusion constant.

4.2.1 Comparison of the Solution of the Random Matrix Equation and the Simulation of the Spiking Network

After having worked out the analytical basis, we compared the prediction obtained from numerically solving (83) for certain spatial configurations of neurons to the steady-state firing rates of the full spiking network with the same spatial structure. In particular, we were interested in the quality of the predictions with respect to the choice of diffusion constant. Figure 30 shows three examples: For D = 10 μm^2/ms, the correlation between measured and predicted firing rates is very good. In contrast, we included the - obviously unsuccessful - attempt to predict firing rates for a simulation with instant diffusion based on the spatial structure by setting D to a relatively high value of D = 100 μm^2/ms. Since instant diffusion overrides any spatial inhomogeneities, this represented a limiting case where our analytic model could not make any meaningful predictions. The outcome of the third case shown in the plot, D = 0, is correctly predicted by the analytic model. In general, instant diffusion as well as D = 0 overrode the effect of spatial heterogeneity onto firing rates. As Figure 31 shows, the actual shape of the distribution was also well predicted by the solution of the linear system. Naturally, these observations led us to the question of how the correlation between predicted measured firing rates behaves in between the aforementioned limits. Especially, we were interested in the range of the diffusion constant for which our model provides a good description of the full spiking

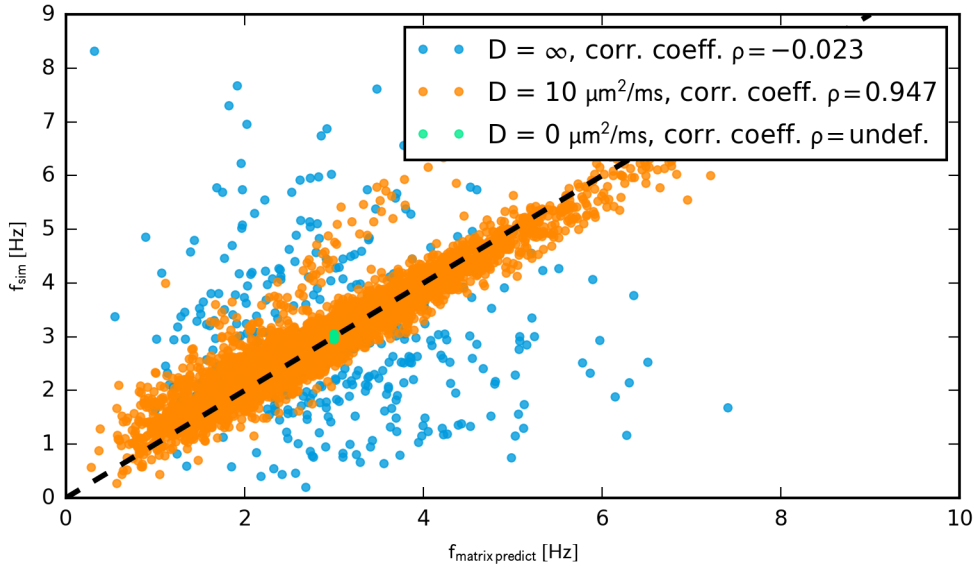

Figure 30: Measured firing rates (t=1200-1500 s) versus predicted firing rates based on the solution of Equation (83). For $D = \infty$ (instant diffusion in the full simulation), the analytic prediction was calculated with a comparably "large" diffusion constant of $D = 100\,\mu m^2/s$.

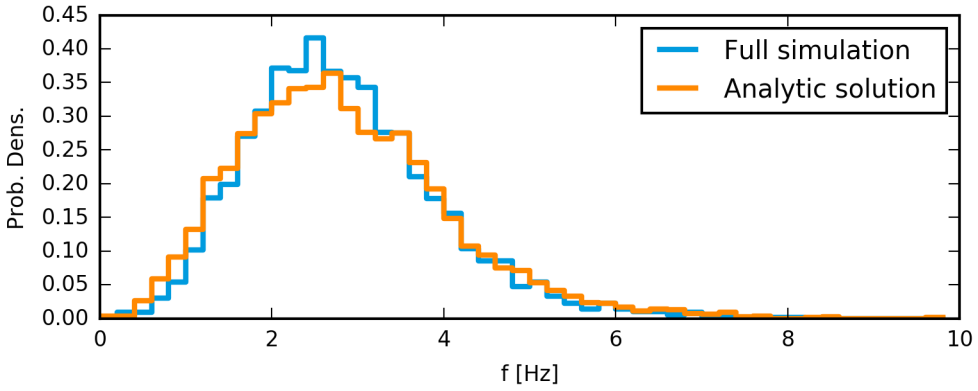

Figure 31: Distribution of firing rates for $D = 10\,\mu m^2/ms$, full simulation and analytic prediction. Data was taken from 10 simulation runs.

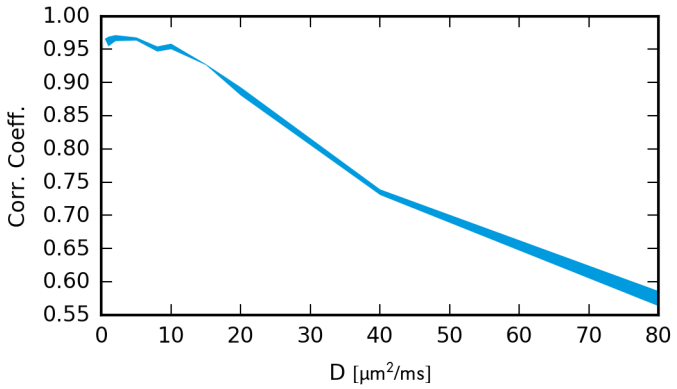

Figure 32: Pearson correlation coefficient of predicted and measured firing rates (see Figure 30) versus diffusion constant. Line width depicts standard error.

network's activity. Figure 32 depicts the Pearson correlation coefficient of $f_{\text{matrix,predict}}$ and f_{sim} against the diffusion constant used in the simulation. A relatively high correlation was obtained for a wide range of diffusion constants. However, we could see a general decline of correlation for larger diffusion constants. This trend was in line with the aforementioned limit of instant diffusion, namely a complete decorrelation between prediction and measurement, as well as the good agreement for $D = 10\,\mu m^2/ms$ shown in Figure 31. We recalled that we characterized the dependence of the shape of the firing rate distribution onto D by means of its standard deviation and skewness in Figure 18. To test whether our analytic model predicts this dependence, we generated random ensembles of neuron positions, solved the linear system of rates and extracted the resulting standard deviation and skewness. Thereby, we found a good fit of the resulting histogram compared to the simulation data, see Figure 33. In summary, shape and broadness of the firing rate distribution appeared to be strongly determined by fluctuation in the spatial distribution of neurons. To further back up this result, we arranged excitatory neurons on a regular grid with a nearest-neighbor distance of $50\,\mu m$ and a $25\,\mu m$ distance between the border and the neurons closest to it. By doing so, all neurons were given the same structure of neighbors. Due to symmetry, we expected that all neurons then should - in theory - exhibit the exact same firing rate. Figure 34 shows the result, being a significantly narrower distribution. This strongly supported the previous assertion.

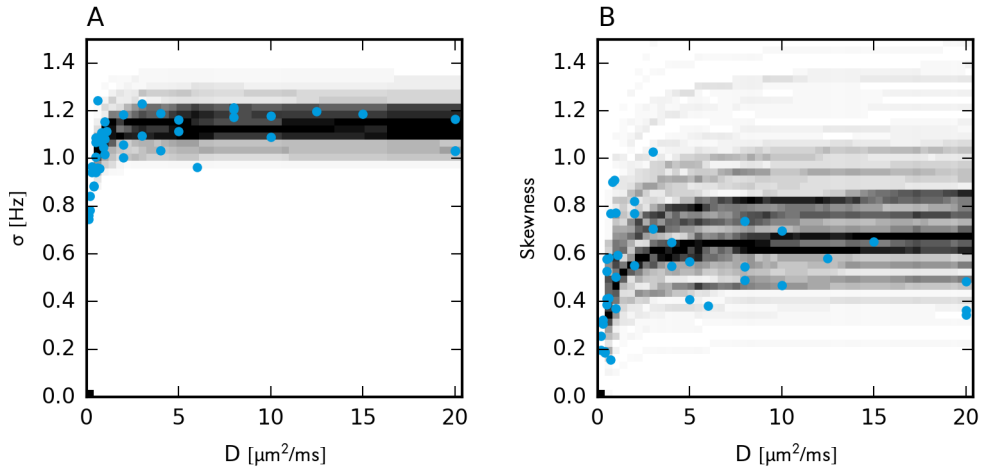

Figure 33: Comparison of distribution of standard deviation (A) and skewness (B) for random-matrix solutions (gray) and values acquired from simulation (blue), Neumann boundaries.

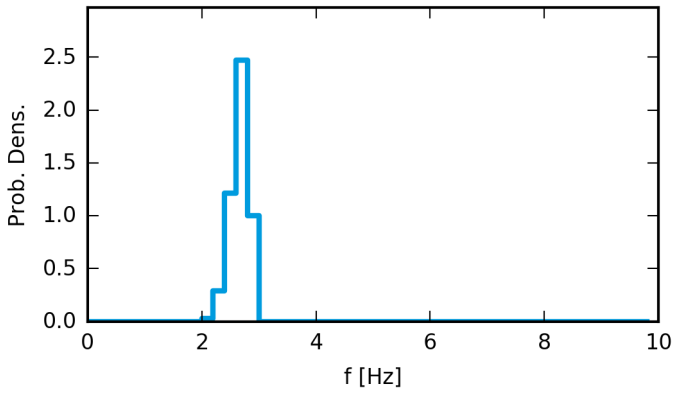

Figure 34: Distribution of firing rates for a regular square grid with distance 50 μm and Neumann boundary conditions, D = 10 μm^2/ms.

4.2.2 Low-Density Neighborhoods correlate with strong outgoing Connections

In Section 3.4.4, we stated that diffusive homeostasis allowed the network do develop few neurons with exceptionally strong outgoing weights. Furthermore, we found this effect to be present in neurons with an highly above-average firing rate. Moreover, the outcomes presented in Section 4.2.1 suggest that the steady state of firing rates is strongly influenced by the spatial structure of excitatory neurons. Combining these two qualities led us the conclusion that one should be able to observe some relation between spatial structure and the emergence of "driver neurons". More specific, regions of neurons with above average firing rates should develop stronger outgoing connections. To get an intuitive understanding of what characterizes regions of above-average firing rates, we interpreted the homeostatic condition in the high-neuron-density limit as an approximation of a continuous integral equation:

$$\int d^2x' \rho(\mathbf{x}') r(\mathbf{x}') \psi(|\mathbf{x} - \mathbf{x}'|) = NO_0 \ , \ \forall \, \mathbf{x} \tag{91}$$

where $\rho(\mathbf{x})$ is the local neuron density and r($\mathbf{x}$) the local firing rate. Here, we assumed that our tissue is of infinite size and thus the integral is carried out over $\mathbb{R}^2$. In this form, the solution for r($\mathbf{x}$) is quite trivial:

$$r(\mathbf{x}) = \frac{NO_0}{\rho(\mathbf{x}) \int d^2x' \psi(|\mathbf{x}'|)} \propto \frac{1}{\rho(\mathbf{x})} \ . \tag{92}$$

Combined with the fact that the logarithm of outgoing excitatory weights correlates with excitatory firing rate (see Figure 26), this led us to the conclusion that low density regions should correlate with strong outgoing weights and vice versa. To test this hypothesis, we approximated the local neuron density by means of a a Gaussian kernel with $\sigma = 50\,\mu$m. Figure 35 shows the results. Despite a certain amount of randomness, our prediction was indeed verified.

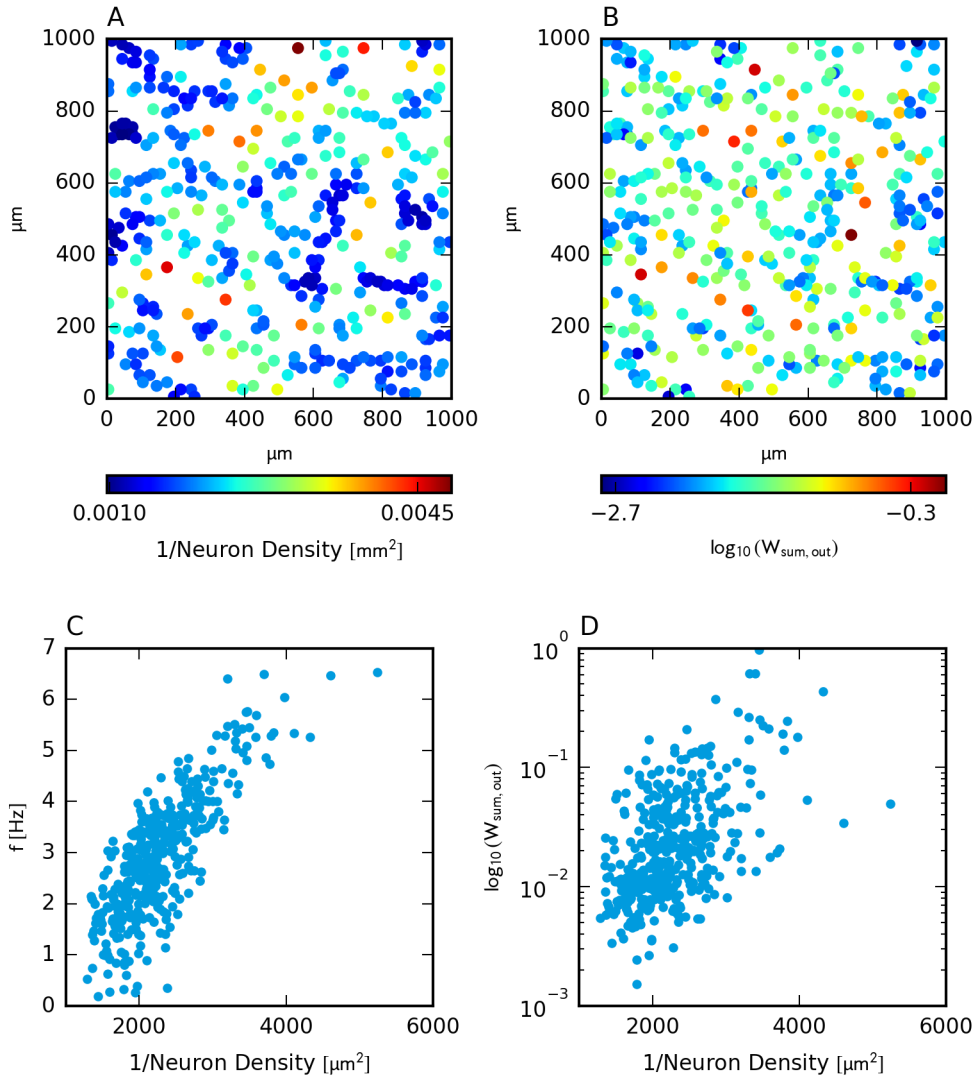

Figure 35: (A) and (B): Scatter-plot of inverse of local neuron density (calculated by convolution with a gaussian kernel with $\sigma = 50\,\mu$m) and decadic logarithm of outgoing excitatory weights. Note the spatial correlation in high/low-density regions. (C) and (D): The decadic logarithm of outgoing weights correlates with inverse neuron density (corr. coeff. of 0.513).

4.3 Spreading of NO-sources extends Encoding of Input Heterogeneity

Since our analytic results revealed that a strong correlation between spatial structure and result firing rates is present if diffusive interaction allows a clear distinction between individual neurons and their spatial neighbors, we considered the possibility that a wider spread of each individual NO-source could locally decrease distinguishability between neurons. Thereby, it might allow input heterogeneities to be encoded over a longer period of time without the need to tweak diffusion to unrealistically high values. The biological plausibility of this idea is discussed in Section 5.2.1.

To test our hypothesis, we modified our model such that each neuron released nitric oxide evenly into a circular area with a radius of 50 μm, centered around the neuron's position. The homeostatic readout was still taken solely from the centering point. Thereafter, we ran the same simulation as for Figure 17. Comparing both plots, we saw a much greater persistence of distinction between excitatory subgroups. The time course of activity suggests that this distinction might even be permanent and steady instead of a very slow but transient state.

5 Discussion

5.1 Homeostatic Stability

Though being unintended in our recurrent network, the occurrence and necessary analysis of persistent oscillations led to a better understanding of their origin and the need for slow timescales of homeostatic adaptation. In another theoretical study, Harnack et al. treated the necessity of slow homeostatic adaptation in a more general fashion [57]. Among other results, it is reported that increasing the number of dynamic variables in a feedback system decreases its stability. This is in line with the fact that our previously used, single-cell homeostatic control (see Equation (10)) exhibited no instabilities, since it only incorporated firing thresholds as dynamic variables. In contrast, diffusive homeostasis increased the dimensionality of the system by means of its NO-synthesis and diffusion pathway. Additionally, Harnack et al. report a similar effect as seen in our system: Noise can reduce stability in a damped dynamical system by constantly causing deviations from its fixed point.

An interesting idea that the aforementioned paper discusses is the possibility that slowness of homeostatic regulation on the timescale of hours might not only be due to functional reasons, such as this rate of adaption being sufficient to compensate for

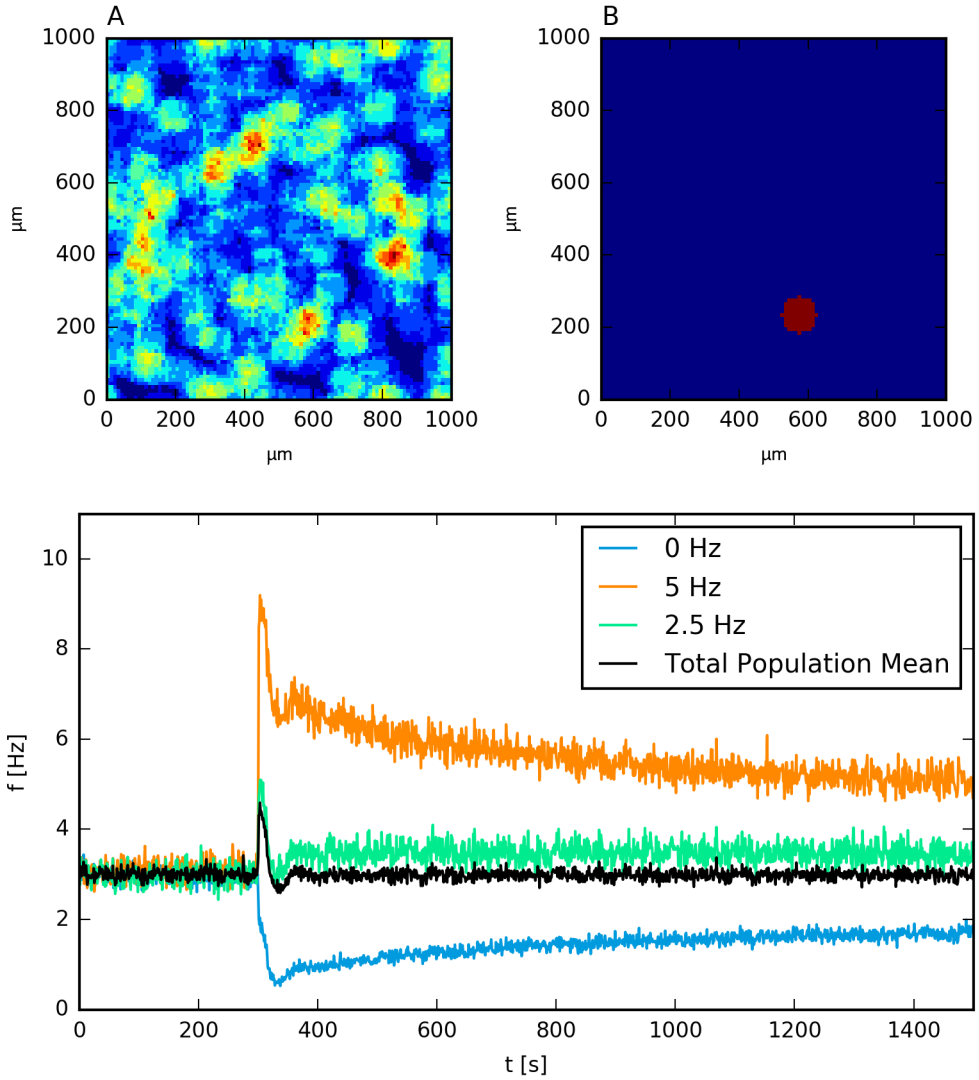

Figure 36: A/B: Illustration of circular kernels used for NO-insertion, overlay of all 400 neurons (left) and a single example (right). C: Resulting activity for excitatory subgroups. All settings were kept the same as for Figure 17.

naturally occurring external perturbations. Based on their analysis, it might also be a mere issue of stability. In the context of this notion, faster homeostatic controls would simply be ruled out because they do not allow the nervous system to stay in a healthy condition. Our findings regarding the stability of diffusive homeostasis thus serves as an example supporting this hypothesis.

5.2 The Firing Rate Distribution

By implementing diffusive homeostasis into the LIF-SORN model we managed to achieve a broader, skewed firing rate distribution while preserving appreciated features of network topology. Though the distribution did approximately resemble a log-normal-like shape, it did not perfectly match our expectations. In order to acquire a deeper understanding of the mechanisms that determine these statistics, we developed analytical expression that allowed us to reliably predict the steady-state of firing rates based on the spatial structure of excitatory neurons. We would like to emphasize that this explanation differs from common approaches of understanding the emergence of heavy-tailed statistics of firing rates in recurrent networks. Theoretical studies on the behavior of recurrent networks are largely based on the assumption that the excitability of neurons is not individually fine-tuned but rather randomly distributed and adjusted globally to achieve a desired mean firing rate. Predictions about the resulting activity are then made based on (potentially simplified) statistical features of recurrent connectivity and the specific form of the neuronal transfer function used in the model, see e.g. [43, 58]. Our interpretation of our results leads to the conclusion that this "canonical" approach matches the limiting case of instant diffusion: While Figures 19 and 15 did not reveal many differences in terms of overall statistics, the decorrelation discussed in Section 4.2.1 and plotted in Figure 32 suggests that increasing the diffusion constant goes along with a transition between a spatially determined configuration of excitatory firing rates and a network topology-determined behavior.

Sweeney et al. claimed that their implementation of diffusive homeostasis enables individual neurons to vary their firing rates more flexible compared to single-neuron homeostatic models, especially allowing for sustained encoding of different levels of external input. Interestingly, we could not confirm this, at least within the tests that we performed and the given set of standard parameters. Overall, the resulting behavior of the excitatory population rather appeared to us as a form of single-neuron homeostasis whose individual targets are predetermined by the quenched random spatial structure of the respective cells. In particular, our result depicted in Figure 17 did not support the notion of separability of inputs. Of course, this impression only applies to the case

where the aforementioned mixture of influence between spatial and synaptic topology is dominated by the former. By analyzing network activity based on our analytic model, we found that for finite diffusion constants, indeed only a single homeostatic fixed point exists. On a practical level though, the gradual decorrelation with this theoretical state of activity upon larger values of D is presumably caused by synaptic turnovers, which change the synaptic input. The resulting changes in activity are more slowly and less accurately compensated in the case of larger diffusion constants. However, for the standard choice of parameters (being roughly based on experimental data), the resulting activity is indeed strongly bound to the spatial structure of excitatory cells. Naturally, this raises the question of biological plausibility. To our knowledge, no experimental study exists that relates measurements of spontaneous activity to local fluctuations of neuronal densities. Ivenshitz and Segal studied the influence of (mean) neuronal density onto neuronal activity in a culture of hippocampal neurons [59]. Lower densities resulted in a more irregular activity, with stronger but less frequent bursting events. However, since our network was tuned to exhibit non-bursting activity, it is hard to draw any conclusions from this result.

From a more general perspective, one could argue that a mechanism binding firing rates to spatial constraints suppresses the ability of the system to adapt to a changing environment since it essentially "freezes" the state of activity. Experiments have shown that neurons' firing rates are indeed correlated under a changing environment/task: Neurons with a certain baseline-firing rate are very likely to have a similar firing rate while performing a task [12]. While homeostatic fixation might not be problematic in the case of transient changes of stimuli, a spatial fixation of firing rates would presumably contradict the fact that long-term learning processes and plasticity lead to persistent changes in activity patterns [60].

5.2.1 Modifications of the Homeostatic Model

Since these considerations evoked a rather skeptical view onto the biological plausibility of these results, we considered possible modifications of the homeostatic model. One should note that these are to be evaluated in the context of providing a model of an actual physiological process. If the main goal was to simply provide a homeostatic method that retains an overall level of activity without tightly fixing individual rates, we would suggest to use the idealized model of instant diffusion, especially because of its computational simplicity. However, as already mentioned, the given experimentally based parameters do not allow to accept this simplification from the standpoint of biological and physical accuracy.

Instead, we hypothesized that by spatially increasing the spread of NO-insertion, we might be able to uncouple activity from spatial structure without tweaking the diffusion process. While Sweeney et al. argued that the size of the studied tissue is large compared to the size of individual somata (which, apparently, they claim to be the main source of nitric oxide), Philippides et al. reported that NO is often synthesized in a more delocalized way by means of fine fibers exceeding the soma [61]. The diameter of these "production areas" is on the order of $10 - 100\mu$m. To incorporate this spread of synthesis in our model of diffusion, we convolved a circular shaped and shifted "production"-kernel (scaled according to the momentary rate of NO-synthesis) with the field of NO-concentration. Intuitively, this locally smeared the distinction between neighboring neurons. From a more abstract point of view, it provided a way to drive the matrix defined in Equation (83) towards singularity, allowing for more states of activity to approximately fulfill the homeostatic target. As Figure 36 suggests, this indeed improved flexibility of individual activity while retaining an overall constant firing rate. By adjusting the area of NO insertion we thereby gained further control over the strictness of the homeostatic mechanism.

Another point of criticism that might justify future changes of the homeostatic model is the plausibility of the used model of threshold adaptation. Experimental studies have investigated the effect of NO onto the conductance of ionic channels [20, 23]. Mapping these features onto a simple LIF-model is obviously not easy, and many consequences of NO-modulation onto neural dynamics can certainly not be represented in such a simple model. Our criticism is thus rather based on more general arguments.

A major issue of Equation (14) is the fact that, given a clamped positive or negative difference between the actual NO concentration and the target concentration, the excitability of the neuron would decrease or increase without bounds. Because of the limited amount of ion channels that exist in a cell and can be affected by nitric oxide, upper and lower bounds should certainly be present. A simple approach to tackle this would be to implement hard bounds into our neuron model, not allowing the threshold to pass an upper and lower value. Another possibility is the implementation of these bounds by means of the differential equation itself. In either case, such a modification could break the ability of the network to tune thresholds in such a way that necessarily *all* neurons eventually reach target concentration. As a consequence, the fixed point of firing rates under diffusive homeostasis would not be strictly determined by spatial structure, but by a combination of network structure and the neurons' positions. As an

example, consider a modification of Equation (14) of the form

$$\dot{V_t^i}(t) = \frac{1}{\tau_{V_t}} \left(\frac{NO(\mathbf{r}^i_{neur}, t) - NO_0}{NO_0} + \frac{\alpha}{V_t^i - V_{t,min}} + \frac{\alpha}{V_t^i - V_{t,max}} \right) . \tag{93}$$

In this form, $\mathrm{NO}(\mathbf{r}^{\mathrm{i}}_{\mathrm{neur}}, \mathrm{t}) = \mathrm{NO}_0$ does not follow any more as the fixed point solution. Rather, one needs to consider the fact that, given the recurrent network topology, the steady state of $\mathrm{NO}(\mathbf{r}^{\mathrm{i}}_{\mathrm{neur}})^* = \mathrm{NO}(\mathbf{r}^{\mathrm{i}}_{\mathrm{neur}}, \mathrm{V}^1_{\mathrm{t}}, ..., \mathrm{V}^{\mathrm{n}}_{\mathrm{t}})^*$ in turn depends on the set of thresholds. Unfortunately, this increase in complexity would presumably make it impossible to find a general analytic description of the fixed point similar to the one introduced and discussed in Section 4.2. Moreover, while this modification would provide a way to incorporate network topology into the theoretical steady state of the system for finite diffusion constants, it is not clear whether it would allow perturbations (e.g. due to external input) to be actually sustained longer.

5.3 Network Topology

Even though our investigations on network topology were rather intended as a form of sanity-check with respect to properties already found in earlier versions, we found some differences compared to non-diffusive homeostasis.

5.3.1 Distribution of Weights

In Section 3.4.2, we presented our results regarding the distribution of weights, which turned out to be broader but still approximately log-normal distributed for diffusive homeostasis. As a first interpretation, we hypothesized that this might due to a slightly decreased amount of STDP-induced potentiation (Figure 21) in the case of diffusive homeostasis in the first half of the simulation. Another explanation one might consider is that the increased firing rate for some neurons in the case of diffusive homeostasis lead to a greater amount of fluctuation because of the increased amount of STDP-events. However, since the overall variance of STDP-induced fluctuations was not significantly higher but even slightly lower compared to non-diffusive homeostasis, this explanation seems rather unlikely.

Taking a closer look at the distributions depicted in Figure 23, we noted that the increased width of the distribution is largely due to to an increment on the left half of the curve. Since new weights are initialized at $10^{-4}\,\mathrm{mV}$, this might indicate that some weights are drifting much more slowly from their value of initialization compared to other weights. These "slow drifters" are presumably connecting neurons both spiking at a below-average firing rate. This provides an explanation why this effect is more present

in the case of diffusive homeostasis since it causes a portion of neurons to have rather low firing rates. On the other hand, for non-diffusive homeostasis, one can assume that the amount of STDP-fluctuations is approximately equal for all recurrent excitatory weights because of the fixation of firing rates.

5.3.2 Strong Differences in Outgoing Weights

The most prominent difference between homeostatic mechanisms we found within network topology was the emergence of significantly above-average mean outgoing weights for a small subset of neurons. By comparing the given mean values to statistics acquired by randomly shuffling recurrent excitatory weights (see Figure 25), we found that this effect cannot be explained by the overall increase of weight heterogeneity that we discussed in the previous section. Thus, we identify the over-representation of strong outgoing weights as a non-random effect. However, we would like to emphasize that diffusive homeostasis is only indirectly responsible in the sense that it allows for a sustained heterogeneity among firing rates.

Referring back to Figure 14, we can now relate the increment of correlation among the excitatory population in the case of diffusive homeostasis to the results discussed in this section: The emergence of very strong outgoing connections increases the probability of neurons being postynaptically connected to such highly influential neurons to fire shortly after the presynaptic neuron. In the light of the notion of "rich get richer" or "rich stay rich" weight-dynamics that were reported for earlier versions of SORN and LIF-SORN, one can argue that this increment in correlation even further stabilizes these strong excitatory weights [25, 26].

As an indirect consequence of spatial structure determining activity (as discussed in Section 5.2), we found that neurons with a low-density neighborhood have a higher chance of developing these strong outgoing weights. Since this effect is directly linked to the low-density/high-firing rate-relation shown in Figure 35 (C), all previous thoughts regarding plausibility similarly apply to this result: *If* a relationship between density and firing rates existed, we could indeed argue to also expect a relation as shown in Figure 35 (D), since it is known that neurons with above-average firing rates tend to undergo long-term potentiation [54, 55].

6 Conclusion and Outlook

Drawing a conclusion from our results presents itself as a somewhat ambiguous task. On a phenomenological level, our main goal of allowing the LIF-SORN to exhibit a broad, skewed distribution was achieved. However, whether the implications of the diffusive model that revealed itself upon deeper investigations are acceptable in terms of biological plausibility is still left open to debate.

Our analysis of the of the feedback control has shown that the dynamics of the system can be approximately described in a linearized way. As we have speculated in Section 5.2.1, a better model of homeostatic feedback might eventually require the introduction of nonlinearity, at the cost of a harder to analyze and predict behavior.

From a topological point of view, the implementation of homeostasis can be regarded as a success: Thanks to the broad range of neural activity it allowed for the emergence of highly influential subgroups of excitatory neurons. This - experimentally confirmed - feature was not present in earlier versions of the LIF-SORN. It thus can be regarded as another non-random property of cortical structure that was not hard-coded but naturally emerged from the set of basic rules that constitute dynamics and behavior of our network.

With respect to future use and implementation of diffusive homeostasis, one might desire to cover the essential effects in a more simple and abstract formalism. As shown in Section 4.1, a simple mean field model as presented by Sweeney et al. still carries problems similar to those of single-neuron homeostasis. However, modifications of this model that incorporates our remarks in Section 5.2.1 might be able to recover properties of the full diffusive homeostatic feedback while being more computationally efficient.

References

[1] Mark F. Bear, B. W. Connors, and Michael A. Paradiso. *Neuroscience: Exploring the Brain*. Lippincott Williams & Wilki, 2007.

[2] Walter B. Cannon. *The Wisdom of the Body*. Norton & Company, 1932.

[3] Bridget N. Queenan, Kea Joo Lee, and Daniel T. S. Pak. Where art thou, homeo(stasis)? functional diversity in homeostatic synaptic plasticity. *Neural Plasticity*, 2012, 2012.

[4] G Turrigiano, LF Abbott, and E Marder. Activity-dependent changes in the intrinsic properties of cultured neurons. *Science*, 264(5161):974–977, 1994.

[5] Juan Burrone and Venkatesh N Murthy. Synaptic gain control and homeostasis. *Current Opinion in Neurobiology*, 13(5):560 – 567, 2003.

[6] Niraj S. Desai. Homeostatic plasticity in the cns: synaptic and intrinsic forms. *Journal of Physiology-Paris*, 97(4–6):391 – 402, 2003. Neuroscience and Computation.

[7] L. Abbott and S. B. Nelson. Synaptic plasticity: taming the beast. *Nature Neuroscience*, 2000.

[8] Peter Dayan and L.F. Abbott. *Theoretical Neuroscience*. MIT Press, 2001.

[9] Holk Cruse. *Neural Networks as Cybernetic Systems*. Brains, Minds & Media, 2006.

[10] G LeMasson, E Marder, and LF Abbott. Activity-dependent regulation of conductances in model neurons. *Science*, 259(5103):1915–1917, 1993.

[11] J. Burrone, M. O'Byrne, and V. N. Murthy. Multiple forms of synaptic plasticity triggered by selective supperssion of activity. *Nature*, 2002.

[12] György Buzsáki and Kenji Mizuseki. The log-dynamic brain: how skewed distributions affect network operations. *Nature Reviews Neuroscience*, 2014.

[13] Adrien Wohrer, Mark D. Humphries, and Christian Machens. Population-wide distributions of neural activity during perceptual decision-making. *Progress in Neurobiology*, 2012.

[14] Gary Marsat and Leonard Maler. Neural heterogeneity and efficient population codes for communication signals. *Journal of Neurophysiology*, 104(5):2543–2555, 2010.

[15] G Turrigiano. Too many cooks? intrinsic and synaptic homeostatic mechanisms in cortical circuit refinement. *Annual Review of Neuroscience*, 2011.

[16] E Marder and J. Goaillard. Variability, compensation and homeostasis in neuron and network function. *Nature Reviews Neuroscience*, 2006.

[17] Yann Sweeney, Jeanette Hellgren Kotaleski, and Matthias H. Hennig. A diffusive homeostatic signal maintains neural heterogeneity and responsiveness in cortical networks. *PLoS Computational Biology*, 2015.

[18] Richard G. Knowles and Salvador Moncada. Nitrix oxide synthases in mammals. *Biochemical Journal*, 298(Pt 2):249–258, 1994.

[19] Richard G. Knowles, Miriam Palacios, Richard M. J. Palmer, and Salvador Moncada. Formation of nitric oxide from l-arginine in the central nervous system: a transduction mechanism for stimulation of the soluble guanylate cyclase. *Proceedings of the National Academy of Sciences*, 86:5159–5162, 1989.

[20] J. Steinert, Cornelia Kopp-Scheinpflug, Claire Baker, R.A. John Challiss, Raj Mistry, Martin D. Haustein, Sarah J. Griffin, Huaxia Tong, Bruce P. Graham, and Ian D. Forsythe. Nitric oxide is a volume transmitter regulating postsynaptic excitability at a glutamatergic synapse. *Neuron*, 60(4):642 – 656, 2008.

[21] J R Lancaster. Simulation of the diffusion and reaction of endogenously produced nitric oxide. *Proceedings of the National Academy of Sciences of the United States of America*, 91(17):8137–8141, August 1994.

[22] Bertil Hille. *Ionic Channels of Excitable Membranes*. Sinauer Associates, 2001.

[23] J. Steinert, S. Robinson, H. Tong, M. Haustein, C. Kopp-Scheinpflug, and I. Forsythe. Nitric oxide is an activity-dependent regulator of target neuron intrinsic excitability. *Neuron*, 71(2):291–305, 2011.

[24] Hans-Christian Pape and Ralph Mager. Nitric oxide controls oscillatory activity in thalamocortical neurons. *Neuron*, 9:441–448, 1992.

[25] Daniel Miner and Jochen Triesch. Plasticity-driven self-organization under topological constraints accounts for non-random features of cortical synaptic wiring. *PLoS Computational Biology*, 2016.

[26] Pengsheng Zheng, Christos Dimitrakakis, and Jochen Triesch. Network self-organization explains the statistics and dynamics of synaptic connection strength in cortex. *PLOS Computational Biology*, 2013.

[27] H Markram. A network of tufted layer 5 pyramidal neurons. *Cerebral Cortex*, 7(6):523–533, 1997.

[28] Sen Song, Per Jesper Sjöström, Markus Reigl, Sacha Nelson, and Dmitri B Chklovskii. Highly nonrandom features of synaptic connectivity in local cortical circuits. *PLOS Biology*, 3(3), 03 2005.

[29] Christoph Hartmann, Andreea Lazar, Bernhard Nessler, and Jochen Triesch. Where's the noise? key features of spontaneous activity and neural variability arise through learning in a deterministic network. *PLOS Computational Biology*, 11(12):1–35, 12 2016.

[30] Romain Brette, Dan Goodman, and Marcel Stirnberg. The brian spiking neural network simulator (version 1.0) [computer software]. `http://www.briansimulator.org/`, 2016.

[31] Li I. Zhang, Li I. Zhang, Huizhong W. Tao, Christine E. Holt, William A. Harris, and Mu-ming Poo. A critical window for cooperation and competition among developing retinotectal synapses. *Nature*, 395:37–44, 1998.

[32] Guo-qiang Bi and Mu-ming Poo. Synaptic modifications in cultured hippocampal neurons: Dependence on spike timing, synaptic strength, and postsynaptic cell type. *The Journal of Neuroscience*, 18(24):10464–10472, 1998.

[33] Robert C. Froemke, Mu-ming Poo, and Yang Dan. Spike-timing-dependent synaptic plasticity depends on dendritic location. *Nature*, 434(7030):221–225, March 2005.

[34] Henry Markram, Yun Wang, and Misha Tsodyks. Differential signaling via the same axon of neocortical pyramidal neurons. *Proceedings of the National Academy of Sciences*, 95(9):5323–5328, 1998.

[35] Barry W. Connors and Michael J. Gutnick. Intrinsic firing patterns of diverse neocortical neurons. *Trends in Neurosciences*, 13(3):99 – 104, 1990.

[36] Jan Benda and Andreas V. M. Herz. A universal model for spike-frequency adaptation. *Neural Computation*, 15(11):2523–2564, 2003.

[37] Niraj S. Desai, Lana C. Rutherford, and Gina G. Turrigiano. Plasticity in the intrinsic excitability of cortical pyramidal neurons. *Nature Neuroscience*, 2:515–520, 1999.

[38] Eugene M. Izhikevich. *Dynamical Systems in Neuroscience - The Geometry of Excitability and Bursting*. The MIT Press, 2007.

[39] AV. Hill. The possible effects of the aggregation of the molecules of haemoglobin on its dissociation curves. *The Journal of Physiology*, 40:iv—vii, 1910.

[40] Andrew Philippides, Phil Husbands, and Michael O'Shea. Four-dimensional neuronal signaling by nitric oxide: A computational analysis. *Journal of Neuroscience*, 20(3):1199–1207, 2000.

[41] Morris W. Hirsch and Stephen Smale, editors. *Differential Equations, Dynamical Systems, and Linear Algebra*, volume 60 of *Pure and Applied Mathematics*. Elsevier, 1974.

[42] Wulfram Gerstner. Time structure of the activity in neural network models. *Phys. Rev. E*, 51:738–758, Jan 1995.

[43] Alex Roxin, Nicolas Brunel, David Hansel, Gianluigi Mongillo, and Carl van Vreeswijk. On the distribution of firing rates in networks of cortical neurons. *Journal of Neuroscience*, 31(45):16217–16226, 2011.

[44] C van Vreeswijk and H Sompolinsky. Chaos in neuronal networks with balanced excitatory and inhibitory activity. *Science*, 274:1724–1726, 1996.

[45] N Brunel. Dynamics of sparsely connected networks of excitatory and inhibitory spiking neurons. *J Comput Neurosci*, 8:183–208, 2000.

[46] Srdjan Ostojic. Interspike interval distributions of spiking neurons driven by fluctuating inputs. *Journal of Neurophysiology*, 106(1):361–373, 2011.

[47] John E. Lisman and Kristen M. Harris. Quantal analysis and synaptic anatomy — integrating two views of hippocampal plasticity. *Trends in Neurosciences*, 16(4):141 – 147, 1993.

[48] Nobuaki Yasumatsu, Masanori Matsuzaki, Takashi Miyazaki, Jun Noguchi, and Haruo Kasai. Principles of long-term dynamics of dendritic spines. *Journal of Neuroscience*, 28(50):13592–13608, 2008.

[49] Yonatan Loewenstein, Annerose Kuras, and Simon Rumpel. Multiplicative dynamics underlie the emergence of the log-normal distribution of spine sizes in the neocortex in vivo. *Journal of Neuroscience*, 31(26):9481–9488, 2011.

[50] Adiel Statman, Maya Kaufman, Amir Minerbi, Noam E. Ziv, and Naama Brenner. Synaptic size dynamics as an effectively stochastic process. *PLOS Computational Biology*, 10(10):1–17, 10 2014.

[51] F. Effenberger and J. Jost. Self-organization in balanced state networks by stdp and homeostatic plasticity. *PLOS Computational Biology*, 2015.

[52] Lina Yassin, Brett L. Benedetti, Jean-Sébastien Jouhanneau, Jing A. Wen, James F.A. Poulet, and Alison L. Barth. An embedded subnetwork of highly active neurons in the neocortex. *Neuron*, 68(6):1043 – 1050, 2010.

[53] J.P. Eckmann, Shimshon Jacobi, Shimon Marom, Elisha Moses, and Cyrille Zbinden. Leader neurons in population bursts of 2d living neural networks. *New Journal of Physics*, 10, 2008.

[54] P. J. Sjöström and G. G. Turrigiano. Rate, timing, and cooperativity jointly determine cortical synaptic plasticity. *Neuron*, 2001.

[55] D. Feldman. The spike-timing dependence of plasticity. *Neuron*, 2012.

[56] Roberto Toscano Couto. Green's functions for the wave, helmholtz and poisson equations in a two-dimensional boundless domain. *Revista Brasileira de Ensino Física*, 2013.

[57] Daniel Harnack, Miha Pelko, Antoine Chaillet, Yacine Chitour, and Mark C. W. van Rossum. Stability of neuronal networks with homeostatic regulation. *PLOS Computational Biology*, 2015.

[58] C van Vreeswijk and H Sompolinsky. Chaotic balanced state in a model of cortical circuits. *Neural Computation*, 1998.

[59] Miriam Ivenshitz and Menahem Segal. Neuronal density determines network connectivity and spontaneous activity in cultured hippocampus. *Journal of Neurophysiology*, 104(2):1052–1060, 2010.

[60] Colin Lever, Tom Wills, Francesca Cacucci, Neil Burgess, and John O'Keefe. Long-term plasticity in hippocampal place-cell representation of environmental geometry. *Nature*, 2002.

[61] Andrew Philippides, Swidbert R. Ott, Philip Husbands, Thelma A. Lovick, and Michael O'Shea. Modeling cooperative volume signaling in a plexus of nitric oxide synthase-expressing neurons. *Journal of Neuroscience*, 25(28):6520–6532, 2005.